Design and implementation of an Atomic Layer deposition System with a coupled in-situ X-ray Photoelectron Spectroscopy tool

Kyle Shiel B.Sc. (Hons)

School of Physical Sciences, Dublin City University

Submitted for fulfilment of the qualification

Master of Science, M.Sc.

September 2021

Dr. Robert O'Connor and Dr. Karsten Fleischer

Declaration

Name: Kyle Shiel

Student number: 14541763

Date: 09/09/2021

I hereby certify that this material, which I now submit for assessment on the programme of study leading to the award of Master of Science (M.Sc.) is entirely my own work, that I have exercised reasonable care to ensure that the work is original and does not to the best of my knowledge breach any law of copyright and has not been taken from the work of others save and to the extent that such work has been cited and acknowledged within the text of my work.

Kyle Shiel

Kyle Shiel

09/09/2021

Date

Table of Contents

List of Abbreviations

Atomic layer deposition	ALD
Atomic Layer Epitaxy	ALE
Binding energy	BE
Chemical vapour deposition	CVD
Energy-dispersive x-ray analysis	EDX
Electron spectroscopy for chemical analysis	ESCA
Hydrofluoric	HF
Kinetic energy	KE
Leningrad Technological Institute	LTI
Molecular beam epitaxy	MBE
Metal–oxide semiconductor field-effect transistor	MOSFET
Metal organic vapour phase epitaxy	MOVPE
Photo-assisted atomic layer deposition	PA-ALD
Plasma-enhanced atomic layer deposition	PE-ALD
Proportional integral derivative	PID
Radical-enhanced atomic layer deposition	RE-ALD
Scanning electron microscope	SEM
Secondary ion mass spectroscopy	SIMS
Trimethylaluminium	TMA
Titanium isopropoxide	TTIP
Ultra-high vacuum	UHV
Ultraviolet	UV
X-ray photoelectron spectroscopy	XPS

List of Figures

Thesis Abstract

Design and implementation of an Atomic Layer deposition System with a coupled in-situ X-ray Photoelectron Spectroscopy tool – Kyle Shiel

Atomic layer deposition (ALD) is an important tool for the research and fabrication of thin-films, used across a wide variety of applications, including the creation of thin metal-oxides, used in the fabrication of high-k semiconductor devices. This scope of this study was to design and build a 'home-made' ALD chamber, with a coupled in-situ X-ray Photoelectron Spectroscopy (XPS) tool, in order to be able to characterise the chemical components of thermally grown ALD films before exposing them to atmospheric contamination. Thermally grown films of aluminium oxide were grown using trimethylaluminium (TMA) as a precursor and H_2O as a co-reactant. These films were grown at differing temperatures and initial surface conditions, in order to test which conditions led to the most ideal films. Titanium oxide films were also grown using a similar method, (employing titanium isopropoxide (TTIP) as the precursor and H_2O as the co-reactant) to ensure the chamber was compatible with a variety of different ALD techniques. While some degree of aluminosilicate growth was observed for all aluminium oxide samples, the growth rates and film compositions for both the TMA and TTIP films were similar to those observed in other studies. These findings show that the system designed works as intended and shows its potential to be used as a process characterisation tool for ALD thin-film processes.

Acknowledgements

Firstly, I would like to thank my family for all their support over the years. To my sister's Niamh and Emma – thank you for the easy laughs, both at you and with you. Thank you to my grandparents, Mick and Alice, for more support and cups of tea than I can count. Most importantly, thank you to my mother, Denise, for the endless encouragement, and for teaching me many valuable life lessons, one way or another.

Thank you to all my friends for their support over the last few years. Alec, Garry and Dayne for their many oohs and aahs; Carol, for listening to many hours of complaints; Aisling, Stuart and Nicola for always having an interesting take, and for at least pretending to read this thesis; all possible members of 43 Cremore Lawn, for many hours of very varying entertainment, and many other friends who deserve a thank you.

Thank you to anyone in the School of Physical Science who helped get this thesis over the line. Thank you to the technical staff of the School of Physics, especially Pat Wogan, for dealing with the many issues that managed to arise. This thesis would not have been possible without you. Thank you also to the Surface Science group, who provided much advice and support over the years, and spent many an hour helping to vent chambers to pick up samples I dropped. Especially Matthew Snelgrove, who surely loaded and unloaded as many samples for this work as I did.

Lastly, I would like to thank Dr. Rob O'Connor for giving me this opportunity, and for his support and experience. Thanks for many hours of fixing my mistakes and clearing confusion. It's been an enjoyable and rewarding experience working in your research group.

1   Introduction

1.1 Thesis Introduction and Project Aims

The focus of this work is to integrate a 'home-built' atomic layer deposition (ALD) with an X-ray photoelectron spectroscopy (XPS) tool, which will be used to grow and analyse Al_2O_3 and TiO_2 films, without the need to expose them to atmosphere before analysis takes place. Atomic layer deposition is a thin-film deposition technique which was adapted from chemical vapour deposition (CVD). ALD uses short, sequential pulses of a (usually metal-organic) precursor which interacts with the surface of a given material. This precursor is then pumped away, and the system is 'purged' of any excess material or reaction products through flooding the system with an inert gas. Once the system is purged, a co-reactant is similarly pulsed into the chamber to react with the adsorbed precursor. The excess of this co-reactant is then also 'purged' from the system and this technique is repeated in a stepwise, sequential fashion, until the desired film thickness is achieved. This 'half-step by half-step' process is used to grow thin-films (usually oxides, nitrides, or metals) at a monolayer scale, allowing for high control over the thickness of the films created. This high level of control makes ALD a powerful tool in the fabrication of microelectronic devices, such as MOSFETs, alongside other uses.

X-ray photoelectron spectroscopy (XPS) is a powerful surface characterisation technique, which employs the quantised energy levels of inner shell electron emission to characterise the atomic composition and state of materials' surfaces. During this technique, the surface of a material is bombarded with x-rays and, through the photoelectric effect, inner shell electrons are emitted from atoms in the sample. These emitted electrons are recorded by a

detector and, through analysis of their kinetic energies, the atomic shell from which they originate can be determined.

The first part of this thesis focuses mainly on the design and characterisation of a home-built ALD system with an in-situ PSP TX400 XPS surface characterisation system. This in-situ XPS system allows for accurate characterisation of the surface chemistry of all ALD processes, while preventing the surface contamination due to exposure to atmosphere which is common in many XPS studies of ALD processes (1). Once this system design was completed, an XPS study of individual Al_2O_3 processes, using Trimethylaluminium (TMA) as the precursor and H_2O as the co-reactant, was carried out in order to better understand the ALD process, and to help to calibrate the individual parameters required for better process optimisation. This was repeated for different sample temperatures, as well as on a hydrofluoric acid (HF) treated, and untreated samples. The growth rate of Al_2O_3 on these samples were then compared with literature values for similarly processed samples, to ensure the process was optimised correctly. A further study of TiO_2 films grown using a thermal ALD process was then completed, with processes carried out on this system, using TTIP as the precursor, and H_2O as the co-reactant, in order to ensure uniform film growth was also possible with other precursors and recipes. This showed that clean uniform film growth was possible for a variety of precursors and allowed for better understanding of process optimisation on this system.

1.2 Thesis Layout

This thesis begins with an introduction to the background and theory of both ALD and XPS respectively, in Chapter 2, in order to ensure the reader has sufficient background in each for future chapters. Chapter 3 describes the design of the ALD system, as well as the electronic components needed, and the initial testing of the ALD valves and heating solutions. An in-depth analysis of the Al_2O_3 process is undertaken in Chapter 4, alongside comparisons of the process with existing literature, with a similar explanation and comparison of the thermal TiO_2 process with literature is completed in Chapter 5. Finally, Chapter 6 contains the discussions and conclusions, as well as suggestions for future work.

2   Theory and Background

2.1   Overview of Atomic Layer deposition processes

2.1.1 Origins of ALD process

Atomic layer deposition (ALD) is an adaption of the chemical vapour deposition (CVD) process that was originally developed, by two independent discoveries, in both Leningrad Technological Institute (LTI) in the Soviet Union (here called Molecular Layering) and at Instrumentarium Oy in Finland (named atomic layer epitaxy) (2). The deposition process of ALD consists of alternating, sequential pulses of a, usually organometallic or metal-chloride, precursor (such as TMA), and a co-reactant, each followed by an inert gas 'purge' to ensure no unwanted reactions between the two. Different co-reactants can be used during the process to achieve different variations of the deposited film. Most commonly, oxides, using an oxygen-based co-reactant (such as water), nitrides, using a nitrogen-based co-reactant (such as ammonia) or metals, using hydrogen-based reducing co-reactants are grown, but sulphides, chalcogenides, and fluorides can also be grown. The design of ALD precursor chemicals is such that they have self-limiting surface reactions, allowing monolayer control of the film growth, as well as creating a uniform, homogenous film over all available surface. This makes ALD a powerful technique in the creation of microelectronic components, as well as for creating films on high aspect ratio structures.

ALD originates from the work of Stanislav Koltsov and Valentin Aleskovsky in LTI in the 1960s. The group originally began with metal chloride reactions, but soon extended to other substrates. These principles (which they coined 'Molecular Layering') were published in a paper in 1967, where TiO_2 and GeO_2 were grown on SiO_2 substrates. This was followed by

Koltsov's professor's thesis in 1971, which led to significant further research of molecular layering by the group, for use in the areas of microelectronics and sorbents and fillers, among others (3).

Shortly after this, in 1974, Tuomo Suntola and Jorma Antson developed atomic layer epitaxy (ALE) for use in thin-film creation of electroluminescent displays. Originally growing ZnS, Suntola and Antson patented ALE as a method of growing thin-films in 1977. In 1985, ALE began to gather interest for use in the deposition of II-IV and III-V compounds (4). Metal organic vapour phase epitaxy (MOVPE) and molecular beam epitaxy (MBE) later replaced ALE as the main growth technique for these compounds due to more favourable surface chemistry.

The two groups met at the first international ALE conference in 1990, and the technique, now referred to as ALD, gained more traction as it was first applied to silicon-based microelectronics and has since become essential for the creation of metal-oxide films for high-k dielectrics and nanostructure fabrication.

2.1.2 Cyclic Process/ Self-limiting Nature

The main difference which separates ALD from conventional CVD processes is the exposure of the substrate to the precursor and co-reactant in a sequential manner, rather than the simultaneous exposure used in CVD. This is helped by the self-limiting nature of the reactants used, allowing the precursor to react completely with the surface, before any excess is 'purged' from the chamber by flowing an inert gas through the system, and the system is evacuated using a vacuum pump. This is then repeated with the co-reactant, and

the process is continued in this stepwise fashion until the desired film thickness is achieved. This sequential, non-overlapping process allows for much greater control over the film thickness than CVD processes, and the self-limiting nature of the chemical precursors employed ensures that a much more conformal film is created.

This binary dose-purge-dose-purge step cycle is usually referred to in each 'half-step', where 'Step A' is the precursor dose and purge and 'Step B' is the co-reactant dose and purge. Each precursor dose step can only react with a finite number of available sites on the surface of the sample, and once these are filled cannot react with itself, causing the reaction to stop. Once the excess precursor is purged from the chamber using an inert gas, the co-reactant is dosed, again only reacting with the available reactive sites, creating a new surface which the original precursor can again react with, allowing the cycle to be repeated. Due to this cyclic process, the growth rate of ALD processes is described in terms of 'growth rate per cycle', rather than the time-based growth rate used to describe CVD processes. The sequential nature of ALD processes also ensure much more uniform films, as each reaction during each step of the process is allowed to be driven to completion before the reactant is purged, ensuring all surface sites have been reacted with, giving a much more homogenous film.
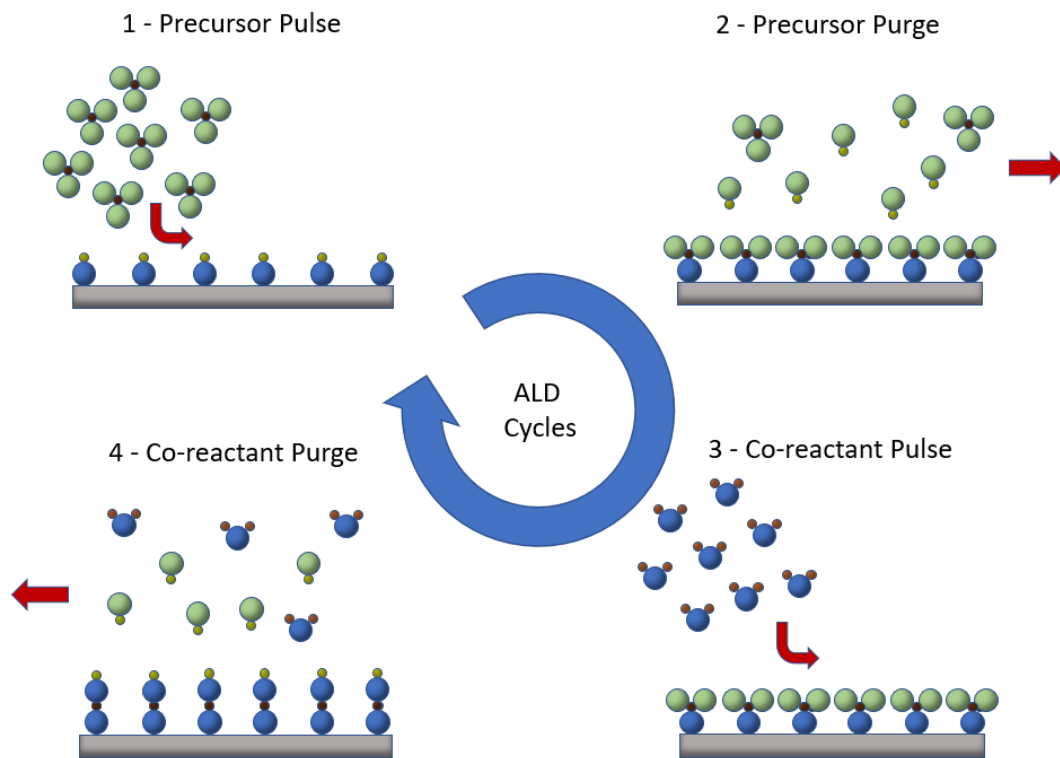
Figure 2.1 Atomic layer deposition process cycle steps

Figure 2.1 shows an example of the cyclic ALD process, where precursor A reacts with an -OH terminated substrate. The precursor is chemisorbed by the heated substrate but cannot react with itself. Any excess unreacted precursor or by-products are purged by an influx of an inert gas. Once the precursor has reacted with all available sites and any unwanted excess pumped away, a new surface has been created. The co-reactant, B (here H_2O) is then pulsed into the chamber, which reacts with the surface created by A. This forms a monolayer of oxygen (or -OH groups), leaving a reactive surface layer for precursor A to react with. All excess and by-products created by the reaction between B and the surface are then purged and the cyclic reaction can begin again. This is repeated until the desired thickness of the film is obtained.

This monolayer coverage per pulse is given by,

$$\theta = (I_i - I_e)\, t_i / \theta_i \qquad\qquad (2.1)$$

where θ_i represents the atomic density for one monolayer of coverage ($\theta = 1$). I_i is the number of atoms impinging on a substrate of unit area per second, I_e is the number of atoms per second reevaporated from the substrate during deposition, and t_i is the pulse length (5). During a pulse, as the number of atoms of the precursor impinging on the substrate, I_i, falls to equal the number of atoms being evaporated from the substrate's surface, I_e, no more deposition can take place. Under ideal conditions, this will mean that all physisorbed A and B species will evaporate off the surface of the substrate during each pulse, leaving only a monolayer of chemisorbed A-B bonds. In reality, due to 'islanding' of precursor during deposition, desorption of precursor during the process, and repulsion between adsorbates, this is not always the case, and only a fraction of the monolayer may be completed during each cycle.

2.1.3 ALD Temperatures

ALD processes are usually carried out at a substrate temperature of approximately 250°C, much lower than the temperatures required for conventional CVD processes. This temperature window, in which reaction saturation is possible and monolayer growth is achieved, is known as the ALD temperature window. Temperatures outside of this window can lead to non-ALD type growth during cycle reactions, which may lead to varying growth-per-cycle during the process, or a less homogenous film, affecting the quality of the material produced. At lower temperatures, surface reactions may be incomplete, leading to a lower

growth rate per cycles and 'pin holing' in the film, which causes much rougher, lower quality film creation. Lower temperatures can also lead to precursor condensation on the surface, which can cause precursor 'islanding', leading to higher growth rates and inhomogeneity of the film. At temperatures higher than the ALD temperature window, precursor desorption may occur leading to precursor atoms leaving their chemisorbed state on the surface, also causing lower growth rates and film 'pin holing'. Higher temperatures can also lead to precursor decomposition, causing unwanted reactions to occur, leading to higher growth rates and less conformal films. To find the ALD temperature window for an individual recipe, the process should be ran at a series of different temperatures, and both precursor and co-reactant pulse lengths in order to ascertain the range best suited for a self-limiting ALD process. Once the pulse length is increased to the limit needed to ensure all available surface sites are reacted with, further increase should, due to the self-limiting nature of the reaction, not increase the growth rate of the film. Likewise, a temperature range where a self-limiting process can be seen, with all non-chemisorbed reactants desorbed from the surface, and a similar growth rate per cycle can be found, showing a steady growth rate per cycle as the film thickness increases. This will ensure that all surface reactions are complete and show that no condensation or decomposition is occurring during the reaction (6). This process optimisation is crucial for the ALD process, as it is necessary to ensure that there is a sufficient amount of precursor available during each pulse to ensure complete film coverage, and also to prevent unnecessary overuse of the precursors due to overly extended pulse times.

2.1.4 Variations of ALD processes

There are four main types of ALD processes which are employed across thin-film deposition. Thermal ALD is the most common of these four and uses a heated substrate in order to obtain the energy required for a surface reaction to take place. These thermal reactions rely solely on the substrates thermal energy to fuel the reaction and are usually based on binary versions of CVD processes. For thermal ALD processes, H_2O or NH_3 are most commonly used as a co-reactant, in order to form oxides or nitrides of the precursor respectively.

The second most common type of ALD process is 'Plasma-Enhanced ALD' (PE-ALD), where a plasma source is used to strike, for example, an O_2 or NH_3 plasma above the substrate surface, incorporating oxygen or nitrogen to the film as required. This plasma step replaces the use of a co-reactant in the process and can be useful as it ensures a more reactive substrate, allowing a wider array of precursors and substrates to be used (7). PE-ALD can also be used when a precursor is water sensitive. It has also been observed to give cleaner, more homogenous films, and reduces the number of by-products produced during the reaction, making it easier to ensure the chamber is correctly purged before beginning the next cycle (7). Finally, PE-ALD can be used at much lower temperatures than thermal ALD, as the energy of the species in the plasma decreases the need for thermal energy to drive the surface reaction.

Another commonly used ALD process is 'Radical-Enhanced ALD' (RE-ALD). Radical ALD is a similar process to PE-ALD, however, instead of striking the plasma directly above the substrate, the plasma is created remote from the surface, allowing only the plasma radicals to react with the surface during the co-reactant phase. While this method provides less incident energy to fuel the reaction than conventional PE-ALD, it also prevents the surface

from being exposed to ion and electron bombardment due to the plasma. Since only the plasma radicals interact with the surface, the film damage which can be caused by the high energy ions and electrons of PE-ALD is prevented (8).

The final commonly used ALD process is 'Photo-Assisted ALD' (PA-ALD). During this ALD process, UV light is shone on the surface. This allows the reactions to take place at a lower temperature, as the reaction mechanic does not solely rely on the substrate's thermal energy to drive the reaction. The energy supplied to the reaction is weaker than that of PE-ALD, and a co-reactant is still required, but it is much easier to control by adjusting the parameters of the UV light used (9).

2.1.5 Al$_2$O$_3$ ALD Process

The TMA-H$_2$O Al$_2$O$_3$ ALD process is one of the most commonly used and well understood ALD processes. It is considered an 'ideal' ALD process and has been studied with a wide range of different process parameters. The variety and longevity of these studies, however, can be somewhat problematic, as interpreting data from a large range of different experimental procedures (different pulse times, substrates, temperatures, etc.) can be difficult. Many of the older studies are also affected by out of date historical assumptions, as explained below, which can also lead to some confusion (10).

2.1.5.1   Process Chemistry

During the TMA-H$_2$O ALD process, the growth of Al$_2$O$_3$ films is progressed through two, self-limiting, 'half-step' processes; one associated with the precursor pulse, and one with the co-reactant pulse. The reactions associated with each of these steps is given by,

$$(A) \quad Al - OH^* + Al(CH_3)_3 \rightarrow Al - O - Al(CH_3)_2{}^* + CH_4$$

$$(B) \quad Al - CH_3{}^* + H_2O \rightarrow Al - OH^* + CH_4 \tag{2.2}$$
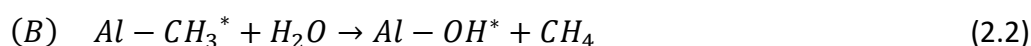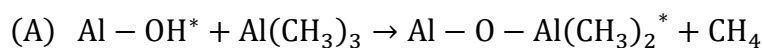
where '*' shows the available surface species (11). When performed as a cyclic process, these reactions will cause the surface of the sample to switch from methyl-terminated (after A) to hydroxyl-terminated (after B) and will continue to grow conformal films of Al$_2$O$_3$ (12). However, studies have shown that the reaction mechanisms of the Al$_2$O$_3$ process is more complicated than these equations imply, showing that the surface -OH concentration can affect the species which are adsorbed. Both the TMA and H$_2$O pulses, while mainly reacting through ligand exchange with the available surface, during their respective steps (both producing methane as a by-product), will also react, through disassociation, with surface oxygen bridges (13).

2.1.5.2   Temperature effects

The Al$_2$O$_3$ thin-film growth window is usually accepted to be between approximately 150 and 300°C, as temperatures higher than this will cause TMA to begin to thermally decompose. However, some studies have shown thermal ALD processes for Al$_2$O$_3$ growth as low as 30°C (12). Most research shows that increasing the substrate temperature for the

process decreases the growth per cycle of the Al_2O_3 film, as long as the reactions are allowed sufficient pulse and purge times appropriate for film growth at the process's respective temperature. Research has shown that the reaction temperature has no effect on the number of aluminium atoms adsorbed during the reaction of TMA with alumina, and therefore, the reaction temperature does not change the mechanisms of the surface reactions during film growth (10). However, increasing the substrate temperature will lead to a variation in the amount of aluminium chemisorbed in a reaction between TMA and the substrate, implying that the temperature of a substrate's surface can have a large effect on TMA adsorption during the initial cycles, as the TMA is reacting directly with the surface of the substrate, rather than with the grown films at the later stages. For Al_2O_3 films grown on Si, for example, the clean Si surface will differ from the Al_2O_3-OH surface (14). This implies that the higher temperature leads to a lower concentration of -OH species on the substrate's surface, causing the lower growth per cycle for the process seen as the temperature increases.

2.1.5.3   Cycle Number effects

The progression of the ALD process causes the surface of the substrate's chemistry to change as the precursor and co-reactant are deposited on it. Due to the non-ideal growth of most films, owing to the varying number of surface -OH species as discussed above, the initial growth stages of the film deposition can have different growth per cycle values than those in the later stages. The growth of films can, therefore, be split into three different growth sections. The first of these sections is the initial pulse, where the first cycle is reacting only with reactive sites on the bare surface. The second is the during the

preliminary cycles, where the precursor and co-reactant is most likely reacting with both the substrate surface, and the surface of the ALD-grown material. The length of this intermittent stage depends on the growth rate of the individual process, as well as the number and availability of reactive sites on the substrates surface. The third stage is in the latter stages of growth, when the reaction is occurring entirely on the ALD-grown surface (15).

These differentially reactive sections of growth lead to three groups of growth type associated with the change from reaction with the substrate's surface, to reaction with the ALD-grown film, linear growth, substrate-enhanced growth, and substrate-inhibited growth. Linear growth occurs when the number of reactive sites on the substrate is equal to the number of reactive sites on the ALD-grown film, which causes the growth per cycle to be constant, regardless of the reaction stage of the growth. Substrate-enhanced growth occurs when the ALD-grown film has less available surface sites than the substrate, causing the growth per cycle of the process to slow after the initial stages of the growth (16). Substrate-inhibited growth, on the other hand, is seen when the deposited film has more reactive surface sites than the substrate, which leads to a lower growth per cycle during the initial stages of the process (16). The growth rate per cycle of both substrate-enhanced and substrate-inhibited ALD will change to become constant once the initial stages of the growth have ended and the film is reacting with the sites on the ALD-grown film only, as shown in Figure 2.2

Studies have shown that the TMA and H_2O ALD process exhibits substrate-enhanced growth when grown on Si surfaces, and will have a higher growth rate per cycle during the initial stages of the reaction (17).
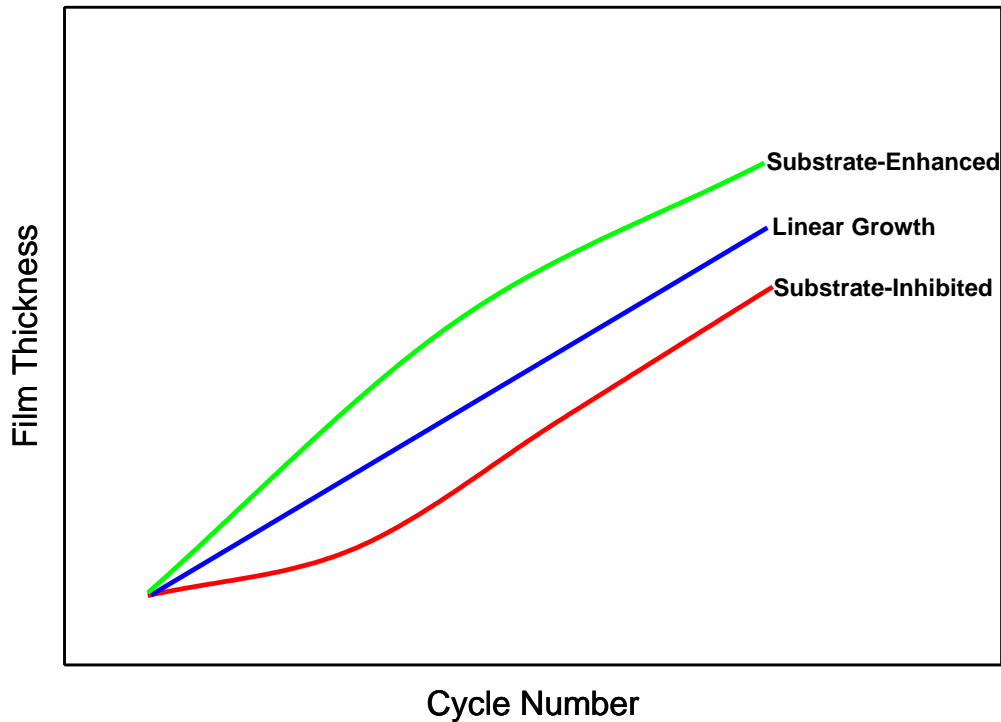
Figure 2.2 Linear, substrate-inhibited, and substrate-enhanced layer growth types

2.1.5.4   Early Assumptions

While ALD processes have been studied from as early as the 1960s, some conclusions made on the basis of experiments conducted during this time have since been proven to not be strictly true, leading to some assumptions which have hindered the understanding of ALD growth. The first of these assumptions is that the growth per cycle of each ALD process is an entire monolayer, which was originally assumed by Suntola and Koltsov in the early 1970s. In reality, many more modern studies have shown that the growth per cycle for most ALD processes (including the TMA-H_2O process) is less than a monolayer (18,19). While gas self-terminating on a solid will, by definition, create a chemisorbed monolayer, this is not necessarily true for the second half of an ALD reaction. This also damages the assumption of "two-dimensional growth" during the ALD process, where, since a monolayer of material is

assumed for each cycle, growth is only measured in the thickness of the film. This assumption ignores the possibility of island growth, which has been seen in many studies (20,21).

The second such assumption which can be harmful to the understanding of ALD growth is that the growth per cycle will remain exactly constant over the growth of the film. This is interlinked with the assumption that a monolayer of material is grown during each cycle. If it is assumed that an entire monolayer is not grown during each cycle, then it can be easily seen that the number of available sites on the surface may fluctuate cycle-to-cycle as the composition of the surface changes (22).

The final assumption historically made about the ALD process is that the temperature of the substrate, within the ALD temperature window, will have no effect on the growth per cycle of the process. However, many studies have shown, as explained above, that the temperature of the substrate may affect the number of available reactant sites on the surface of the sample. This, coupled with the varying number of available sites due to inexact monolayer growth, causes lower growth rates per cycle during lower temperature processes. The TMA-H_2O process has also been shown to have lower growth rates at lower temperatures (10). This effect has since been extensively studied, and the assumption has been mostly abandoned by many studies.

2.1.6 Al$_2$O$_3$ Applications

ALD deposition of Al$_2$O$_3$ has a wide range of applications, available across microelectronics, protective coating, and solar cell production. The use of Al$_2$O$_3$ in the production of high-permittivity gate oxides is one of the most widely studied areas of ALD. Deposition of Al$_2$O$_3$ on SiO$_2$ gate dielectric MOSFETs can help prevent tunnelling current through the gate dielectric when it is built on a typical large-scale microelectronic processing scale (<1 nm). Al$_2$O$_3$'s higher dielectric constant allows for thicker gate dielectrics to be made for the required capacitance density, which helps to prevent electron tunnelling in the gate (23). Al$_2$O$_3$ has also been used as a thin, uniform insulating material in magnetic recording heads, due to its high accuracy thickness control, allowing for better quality recordings (24), as well as being used as a protective coating for copper surfaces (25). Newer studies have also shown the use of Al$_2$O$_3$ as a solution for the passivation of *p-* and *n-*type Si surfaces, in the production of solar cells (26). This shows that the production of Al$_2$O$_3$ films, while well studied, is still a vibrant and important area of ALD research.

2.1.7 TiO$_2$ ALD Process

As with the TMA-H$_2$O Al$_2$O$_3$ process, the downscaling of electronic components has led to an increase in interest in many other ALD precursors and recipes. One such process, which has been extensively researched, is the fabrication of TiO$_2$ thin-films from various precursors and co-reactants. While a large variety of precursors and co-reactants are well studied for the production of TiO$_2$ films, the use of titanium tetraisopropoxide, or TTIP, as a precursor and water as a co-reactant is one of the more common routes, as it has shown to be a stable thin-film production technique (27). During the TTIP-H$_2$O process, as explained above, the

growth of TiO$_2$ films is advanced through the use two 'half-steps', one being the introduction of the precursor, which is then purged before the co-reactant is introduced, repeated in a cyclic pattern. The process chemistry for this reaction is given by,

$$(A) \quad Ti-OH^* + Ti\{OCH(CH_3)_2\}_4 \rightarrow Ti\{OCH(CH_3)_2\}_3^* + (CH_3)_2OHCH$$

$$(B) \quad Ti\{OCH(CH_3)_2\}_3^* + H_2O \rightarrow Ti-OH^* + (CH_3)_2OHCH \tag{2.3}$$
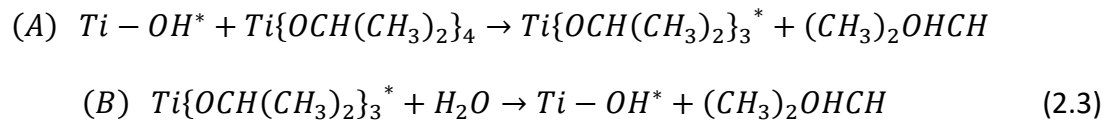
where '*' shows the available surface species (28). Similar to the Al$_2$O$_3$ process, these reactions will cause the surface of the sample to switch from methyl-terminated (after A) to hydroxyl-terminated (after B).

TTIP has a similar temperature window to the TMA thermal process, with the growth window usually seen to be between 150-300°C, with some decomposition seen above 300°C, and notable decomposition seen above 350°C. Films grown below these temperatures show a notable drop in both growth rate and film quality and homogeneity (27,29). As discussed above, due to the non-ideal growth of most ALD films caused by a varying number of surface -OH species, the growth rate per cycle for this thermal TiO$_2$ process varies slightly when comparing the initial stages of the reaction and the later cycles. However, while the initial stages of the process (<5 cycles) do show a slightly lower growth rate per cycle, this substrate-inhibited growth is likely due to the lower number of reactive sites available on the bare surface than on the TiO$_2$ film, and after the initial interaction between the precursor and the surfaces reactive sites the growth rate stabilises as the film begins to grow (30).

2.1.8 TiO_2 Applications

TiO_2 films have been widely studied for a great range of different applications, including applications in semi-conductors, as nano-paint, in the production of nanotubes, and in photocatalysis. It's electrical, optical, and morphological properties make thin-films of TiO_2 an ideal candidate for many environmental applications. TiO_2 is especially of interest in the photocatalysis and semi-conductor areas due to its low cost, high efficiency and photochemical stability (31). While photoactivity in TiO_2 thin-films is only seen under UV radiation, doping these thin-films with nitrogen ions or certain metal oxides has been shown to enable excitation even under visible light (32). TiO_2's ability to be grafted onto various organic compounds, which can improve the materials light absorption abilities, as well as its non-toxicity, also allow for use in medical applications, such as targeted therapy (33). This, along with the creation of titania nanotubes, has led to an increase in research into TiO_2 in biomedical application (34). As can be seen, TiO_2 thin-film growth is still an area of great interest to many different industries and an important are of ALD research.

2.2 Overview of XPS

2.2.1 Introduction to XPS

In the early 1900s, following Albert Einstein's explanation of the photoelectric effect, P.D Innes recorded broad-band electron spectra as a function of velocity using a Röntgen tube, Helmholtz coils, a magnetic field hemisphere, and photographic plates. Kai Siegbahn's group in Sweden, expanding on the work done by P.D. Innes, improved the equipment greatly, and performed high-resolution x-ray photoelectron spectroscopy (XPS) for the first time, using cleaved sodium chloride, in 1954. In 1967, Siegbahn released a detailed study of XPS and, working with a group of engineers at Hewlett-Packard, produced the first monochromatic XPS instrument in 1969.

XPS relies on the photoelectric effect, in which a material irradiated by x-rays of a constant energy, *hv*, will cause electrons in the core levels of the material's atoms to be ejected, providing the x-ray energy is higher than the electron binding energy in the material. Since energy in the system is conserved, the binding energy of the emitted electrons can be found using the equation:

$$KE = hv - BE - \phi \qquad (2.4)$$

where *KE* is the kinetic energy of the emitted electron, recorded by the detector, *hv* is the incident x-ray energy, *BE* is the electron's binding energy, and ϕ is the work function, a correction factor used to account for the small amount of kinetic energy given up by the emitted electron as it is absorbed by the detector (35). Figure 2.3 shows the kinetics of electrons being emitted from the core levels of an atom due to the photoelectric effect.
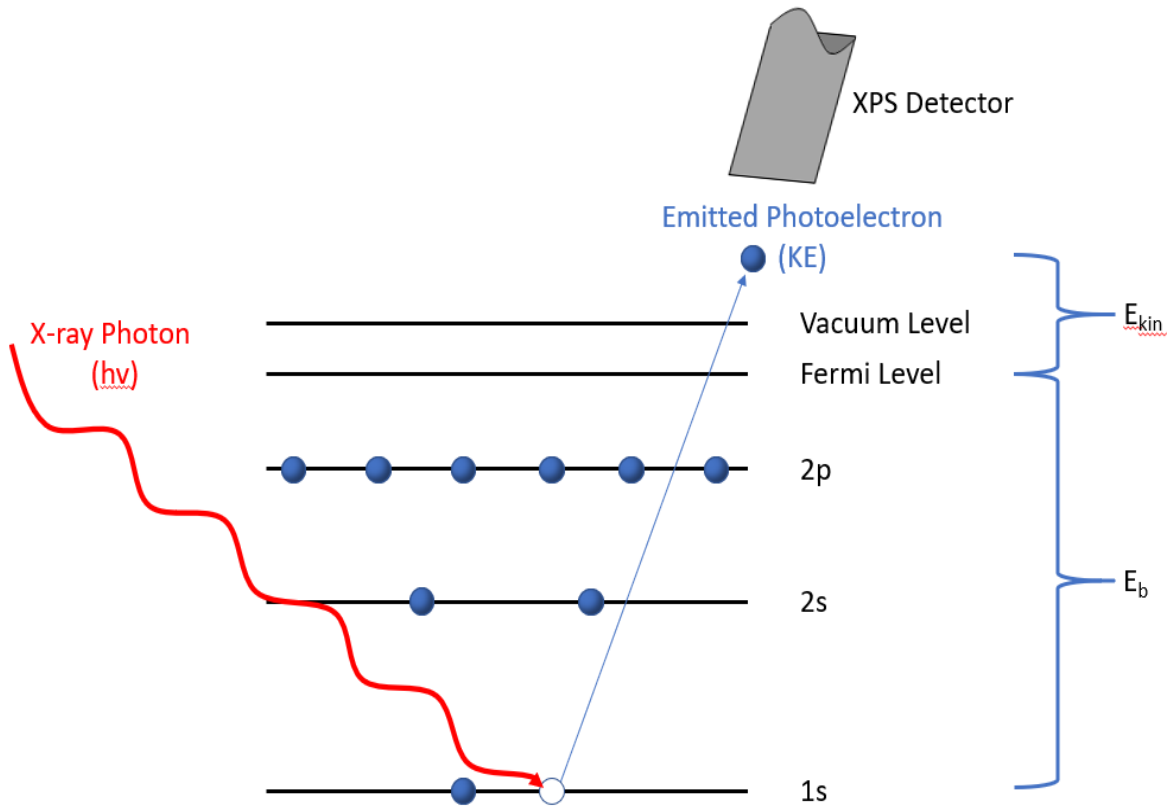
Figure 2.3 X-ray photoelectron spectroscopy electron emission kinetics

This is useful for material characterisation as electrons are emitted from particular atomic core levels, known as the *s*, *p*, *d*, and *f* subshells, and so will have well defined binding energies, unique to each atom. Due to the energy of the incident x-rays being kept constant, and the work function change being negligible, the recorded kinetic energy of an emitted electron will also be well defined and can be used to determine the atomic element, and core level from which it was emitted.

2.2.2 Sampling Depth and Inelastic Scattering

Incident high energy x-rays (>1000 eV) can penetrate a material up to a depth of several microns. XPS however, can only record the atomic characteristics of approximately the first 10 nm of a substance, due to inelastic scattering of emitted electrons within the sample. Once an electron has been emitted from an atom's core shell, it must travel through the material before having its energy characterised by colliding with the XPS detector. These electrons may interact with atoms within the material, leading to elastic or inelastic scattering, depending on whether their kinetic energy changes, as shown in Figure 2.4. Electrons which undergo inelastic scattering within the sample, before colliding with the detector, cannot be used for surface characterisation, as they will not retain the quantised energy associated with their emission from an atomic shell and so become part of the XPS background spectrum. The probability of inelastic scattering occurring within a material is dependent on both the energy of the electron and the material through which the electron is travelling. This is given by the equation:

$$I(x) = I_0\,exp\left(\frac{-x}{\lambda(E_k, Z)}cos\theta\right) \tag{2.5}$$

Where $I(x)$ is the electron intensity after travelling through a material of thickness x, I_0 is the initial electron intensity, θ is the angle of emission with respect to the surface normal, and $\lambda,(E_k, Z)$ is the electron escape depth and represents the depth at which photoelectrons have a probability of 1/e of escaping the sample without losing energy. Electrons in this energy range (50-1000 eV) typically travel up to 10 nm before losing energy through inelastic scattering in a given material, which gives XPS its maximum characterisation depth (36).
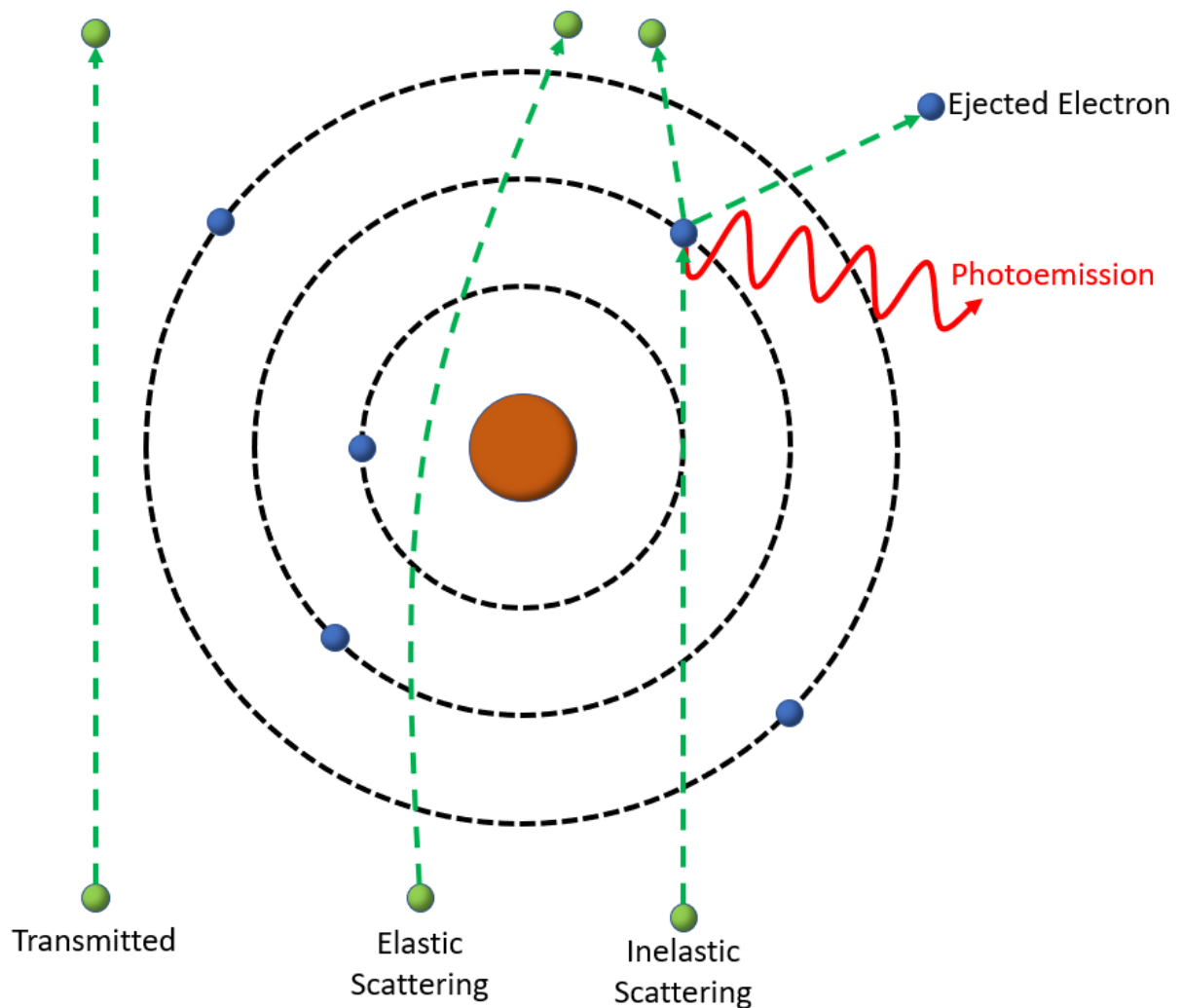
Figure 2.4 Emitted electron scattering interactions

2.2.3 Twin Anode and Monochromated Sources

In older XPS systems, such as the one fitted to the custom ALD system built during this work, x-rays are created using a twin anode x-ray source. During x-ray generation, one of the two anodes (usually aluminium and magnesium) is bombarded with electrons, which generates x-rays. The source is housed with a thin aluminium window, which allows x-rays to pass through, while protecting the sample from the fields generated by the source, as well as suppressing the background bremsstrahlung radiation, and preventing filament

contamination. However, when using twin anode sources, a small number of x-rays can be produced by the second anode source, even when not in use. When this occurs, the x-rays produced by the second anode will have a different incident energy than those created by the first, corresponding to the material of the anode (1254 eV for Mg and 1487 eV for Al, for example). The electrons emitted from the similar core levels within the sample will therefore have different kinetic energies, depending on which anode's x-rays they are excited by, as seen in Equation (2.4). These differing kinetic energies will cause 'ghost peaks' to be seen, as the energy recorded by the detector will show different kinetic energies for the same core levels, depending on the source of the incident x-rays (37).

Modern XPS systems, on the other hand, such as the industrial tool used for comparison in this work, make use of monochromated x-ray sources, which use only one anode. In a monochromated x-ray system, created x-rays are reflected off a quartz crystal. As the incident x-rays are reflected off the parallel planes within the crystal, constructive interference occurs. This focusses the x-rays more precisely on the sample, leading to narrower XPS line widths, a lower spectral background, and a complete elimination of unwanted x-rays from satellites and anode impurities, when compared with older twin anode systems (38).

2.2.4 Photoionisation Cross-Sections

The photoionisation cross-section (σ) is defined as the transition probability per unit time for excitation of a single photoelectron from the core level of an atom under an incident photon flux of $1s^{-1}cm^{-2}$ (39). It is the number of electrons emitted from an atomic core level per unit time, depending on the incident x-ray energy hv.

For monochromated x-ray sources used in XPS systems, high energy electrons are focussed on a water-cooled metal anode. This metal anode produces high-energy, non-monochromatic x-rays, which are focused through a quartz crystal. The metal used for the system's anode will determine the photon energy (hv) of the x-rays produced. Most commonly, magnesium (Mg Kα) or aluminium (Al Kα) are used, which have photon energies of 1254 eV and 1487 eV respectively. The cross-section for every element using these two photon energies was calculated by Scofield in 1976 (40). This Scofield table, which references an element's cross-section against that of the C*1s* peak (which has a cross-section of 1), is still the most commonly used reference during XPS surface characterisation. Through identifying the individual elements in the sample, and using the Scofield table, the percentage elemental composition of a material can be estimated by dividing the peak heights by their elemental cross-sections and finding the percentage of the total adjusted peak intensity, as shown in Equation (2.6).

$$\text{Adjusted Peak Intensity} = \frac{\text{Recorded Peak Intensity}}{\text{Element cross} - \text{section}}$$

$$Composition\ \% = \frac{Adjusted\ Peak\ Intensity}{Sum\ of\ Adjusted\ Peak\ Intensities * (Kinetic\ Energy)^{0.7}} * 100 \qquad (2.6)$$

Dividing the adjusted peak intensity by $E_{kin}^{0.7}$ helps to 'normalise' the peaks. This is necessary to account for the difference in wavelength due to different photon energies. This helps adjust for the variation in the mean free path associated with electrons being emitted at different energies, as the number of electrons recorded for an emission peak reduces due to the volume of material from which an electron can emerge without inelastic scattering reducing as the kinetic energy of the electrons decreases (41). This normalisation allows for more accurate comparisons of peaks with a large difference in binding energy.

2.2.5 Chemical Shifting

It is also possible to identify the chemical state and chemical bonding characteristics of atoms in a material using XPS. This is due to the "chemical environment" of an atom influencing the binding energy of its electrons. Electrons in the core shells of an atom are affected by both their attraction to the positively charged protons in the nucleus, and by their Coulomb interaction with other electrons. This "chemical environment" of an atom is affected by the atom's oxidisation state, the identity of its nearest neighbour atom, and its bonding hybridisation to its nearest neighbour atom. A change in any of these will cause a redistribution in the atom's valence electron charges, leading to the core electrons experiencing a different Coulomb potential and, therefore, having slightly shifted binding energies (42). Figure 2.5 shows the Si2p element peak, plotted alongside its oxidised equivalent. Through analysis of these binding energy shifts and peak fitting software, XPS can be used to find the bonds and oxidisation states of atoms within analysed material.
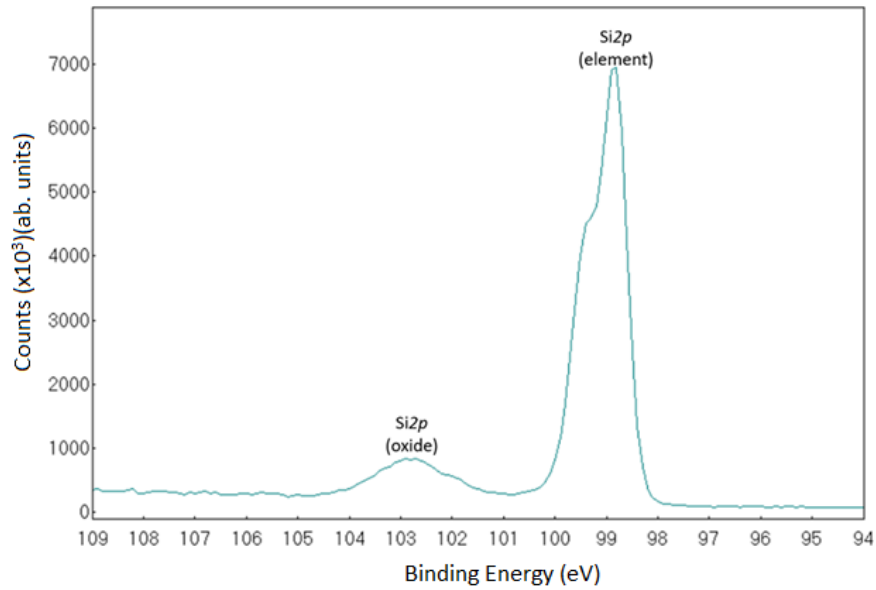
Figure 2.5 Si2p element and oxide XPS spectrum of an unprocessed Si sample with native oxide

2.2.6 Sample Charging

During XPS analysis, samples are bombarded with ionising x-rays which release electrons from the surface of the sample. Photoelectron - and secondary electron emission, if the sample has insulating properties - may cause positive charging within the sample, as the insulating material will not have a sufficient number of free electrons for electron-hole recombination to occur. Also, when using a monochromated x-ray source, an insufficient number of electrons will be retained in the region of the sample to limit the effects of the sample charging (38). This charging can cause the spectrum peaks to become shifted to higher binding energies and may lead to spectra distortion. To combat this issue for insulating samples, or if the system's geometry does not allow for sufficient grounding, an external electron source is most often used to replenish surface electrons, neutralising

charging effects. The most common charge neutralisation tools are low voltage electron flood guns (0-20 eV), UV light sources, or low voltage argon ion coupled with low-voltage electron beams (42).

Due to the possibility of differing peak binding energy due to chemical shifting, as explained above, charge reference peaks are used to ensure the electron binding energies are shifted correctly. The most commonly used charge reference peak is the C$1s$ peak. The binding energy of the C$1s$ peak is usually taken to be 284.8 eV and is used due to the presence of adventitious carbon on all air-exposed conductive and semi-conductive materials. Recent studies, however, have shown some doubt in the use of the C$1s$ peak alone as a charge reference peak, due to the effect of carbon adsorption inside vacuum systems, as well as the effect of different substrates on the chemical nature of adventitious carbon (43).

2.2.7 In-Situ Characterisation

As discussed briefly above, exposure to atmosphere can lead to adventitious carbon and oxygen depositing on the surface of the sample. During XPS analysis, which is primarily a surface characterisation tool, these surface contaminants can play a large role in the analysis of a material.

Figure 2.6 shows recorded XPS spectra for a TiO$_2$ film deposited by atomic layer deposition taken both in-situ, and after a short (~5min) atmospheric exposure of the sample. As can be seen, both the oxygen and carbon peaks show intensity increases, as well as changes to the binding energy shifts and the respective peak profile after exposure to atmosphere. The peak broadening seen in both spectra is consistent with the peak positions of C-O and C=O

bonds in the carbon spectrum, and -OH bonds in the oxygen spectrum, all of which are associated with surface contamination due to atmospheric exposure. As XPS spectroscopy is often used when the oxygen and carbon peaks are of particular interest, this contamination can easily skew results. This result shows the importance of in-situ film characterisation, both to ensure the correct characterisation of the deposited films, and to ensure prevention of film contamination during XPS measurements taken between growth cycles. In order to gain a true understanding of the surface chemistry that underpins ALD reactions, and to effectively characterise processes and precursors, in-situ characterisation is crucial as it allows for spectra to be acquired during the film growth which represent the true nature of the films. Furthermore it facilitates a better understanding of the film's surface chemistry during nucleation and subsequent growth (1).
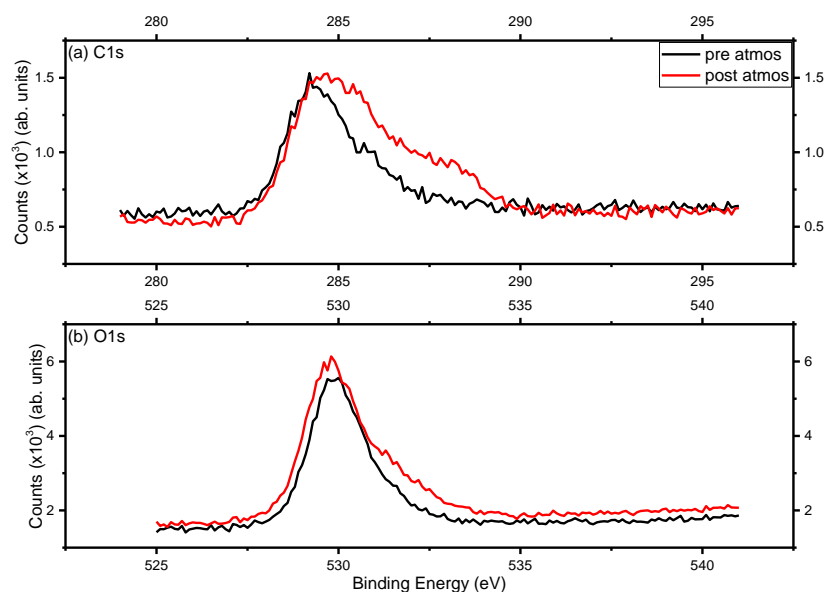

Figure 2.6 In and ex-situ high resolution XPS spectra of: (a) the C1s peak, and (b) the O1s peak of a 1 nm TiO₂ film grown using a TTIP precursor and H₂O co-reactant on native oxide Si, with a substrate temperature of 200°

3 System Design

3.1 Basic Chamber Design

The primary concern behind the basic design of the ALD chamber presented in this work was to allow the self-limiting nature of the ALD process to be observed, while also allowing for transfer of samples between the ALD reactor and the UHV-XPS chambers without contamination of the XPS chamber due to the ALD reactants. For this to be possible, the ALD and XPS chambers needed to be isolated from one another. The ALD sample-stage also needed to be able to hold 'ESCA style' sample stubs which were compatible with the XPS system, while also providing a sufficient sample heating solution.

The basic design of the ALD system involved using a spherical Kurt J. Lesker vacuum chamber, fitted with a roughing-backed TurboVac 361 turbo vacuum pump. These pumps allow the pressure in the chamber to reach 1×10^{-6}mbar while idle, which facilitates relatively rapid transfer of samples between the two vessels. This turbo pump, which is backed by an Edwards RV5 rotary pump, can also be isolated during depositions in order to prevent a build-up of deposited materials on the turbo pump blades. During depositions, the chamber is opened to a separate Edwards LZM rotary roughing pump in order to keep the pressure in the chamber low enough to ensure no contamination due to air on the sample. Pirani and Penning gauges are also used to record the pressure in the chamber, both during depositions and under normal conditions, respectively. A Pirani gauge is used during depositions as the pressure range during depositions is within the Pirani gauge's range, and the fast response time allows the change in chamber pressure during pulses to be observed, while the Penning gauge is used when the chamber is idle to ensure the pressure in the chamber was sufficiently low and all process chemicals have been removed

from the chamber. A loadlock and attached magnetic transfer arm are attached to the ALD chamber, directly opposite the XPS chamber opening, allowing for transfer of samples between all three chambers. Both the loadlock and XPS chambers are fitted with gate valves, allowing each chamber to be isolated from the others, in order to prevent chamber contamination due to atmospheric exposure while loading or unloading samples, as well as during ALD processes. Wobble sticks are also fitted to both the ALD and XPS chambers to allow transfer of samples between the transfer arm and the respective chamber stages. Inlet pipes are fixed to the top of the chamber, through which the ALD process precursor and co-reactants, as well as the inert 'purge' gas, are admitted to the chamber. Figure 3.1 shows a schematic of the basic design of the ALD chamber.

Front View

To Piping

Sample Stub

Manipulator Arm

Wobble Stick

Roughing Pump
Isolation Valve

Sample Holder

To Temperature Control

Turbo Isolation Valve

To Roughing Pump

Turbo

Side View

Sample Stub

Chamber Gate
Valve Control

Loadlock

Chamber Gate
Valve

To XPS
Chamber

Transfer Arm
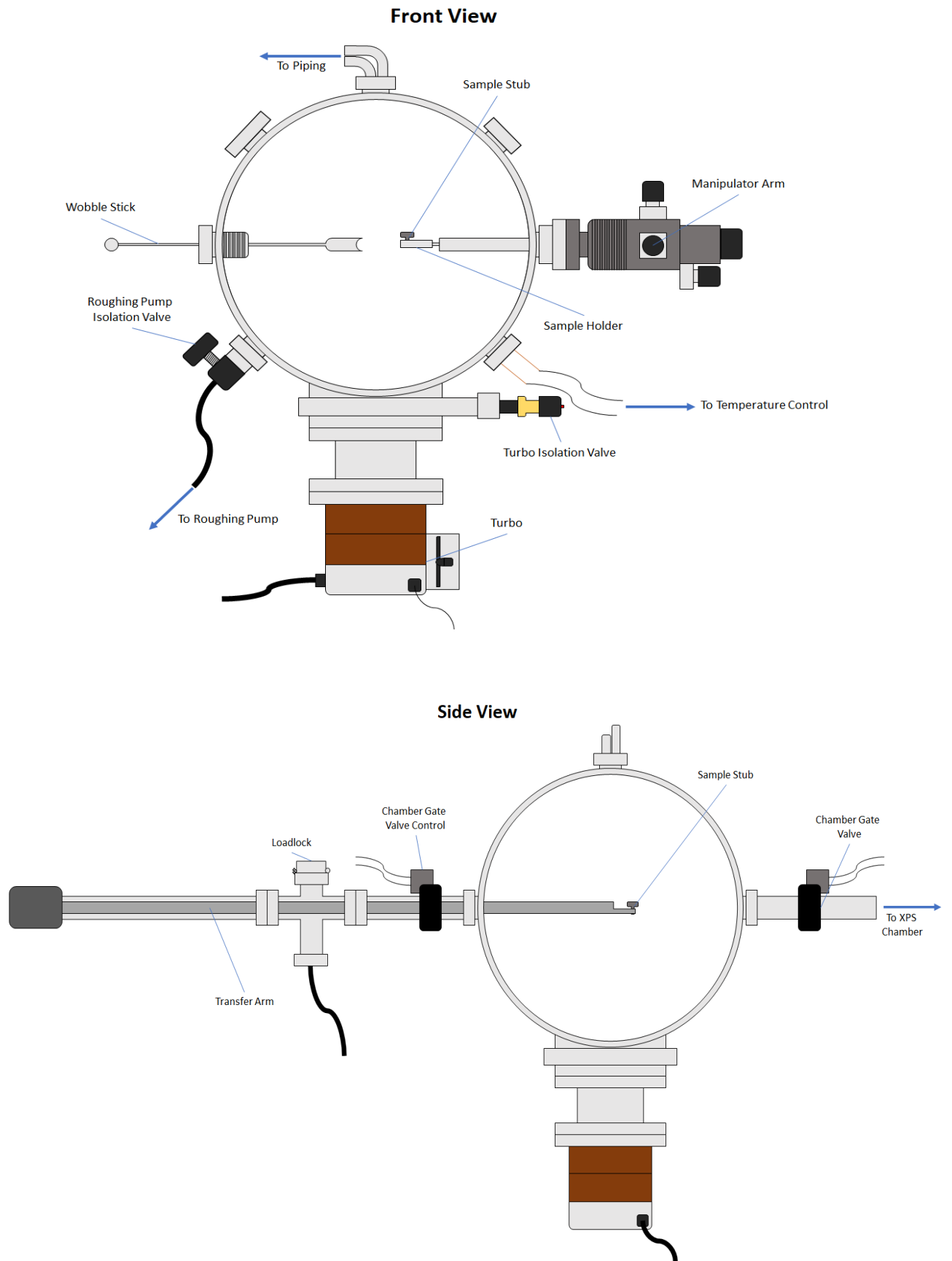
Figure 3.1 Front and side view schematic of ALD chamber design

3.2 Sample Heating and Stage Design

One of the most important aspects of the ALD system design was ensuring efficient and well controlled sample heating. As discussed above, for a thermal ALD process to exhibit monolayer growth, the substrate surface must be within the 'ALD temperature window'. The sample stage therefore needed to be able to both hold the 'ESCA style' sample stubs used in the XPS system, and also provide heating to the sample. Samples were attached to 'ESCA style' sample stubs and were secured with silver paste, which both secures the sample to the stub, and also ensures good thermal conductivity between the stud and the sample. Figure 3.2 shows the sample stage design used for this ALD system. A small hole in the top allows a sample stub to sit into the stage. Aluminium was chosen as the material for the sample stage, as it ensures a good thermal conductivity between the heater and the sample. A $2cm^2$ ceramic heater, coupled with a thermocouple, was attached to the bottom of the stage, with screws to hold it in place. This ceramic heater was chosen as appropriate, as it would work efficiently under high vacuum, would not be damaged during the depositions, and could be safely heated up to 600°C. An Arduino controlled proportional integral derivative (PID) code was used to control the temperature. PID uses a control-loop feedback mechanism to control variables (here temperature) and is used to ensure accurate, automatic control of the temperature of the sample to within 0.1 °C. A 40V power supply was used to power the ceramic heater and was attached through a PID controlled transistor, and a MAX6675 board was used to allow the Arduino to read in the thermocouple data. This sample stage was placed on a manipulator arm, allowing for movement of the stage to help with sample transfers and to ensure the stage was not obstructing transfers to the XPS chamber. This also allowed the sample to be moved to

different positions in the chamber for depositions, ensuring that the process yielded similarly grown films, regardless of the orientation of the sample.

Top View

Bottom View

Front View

Side View
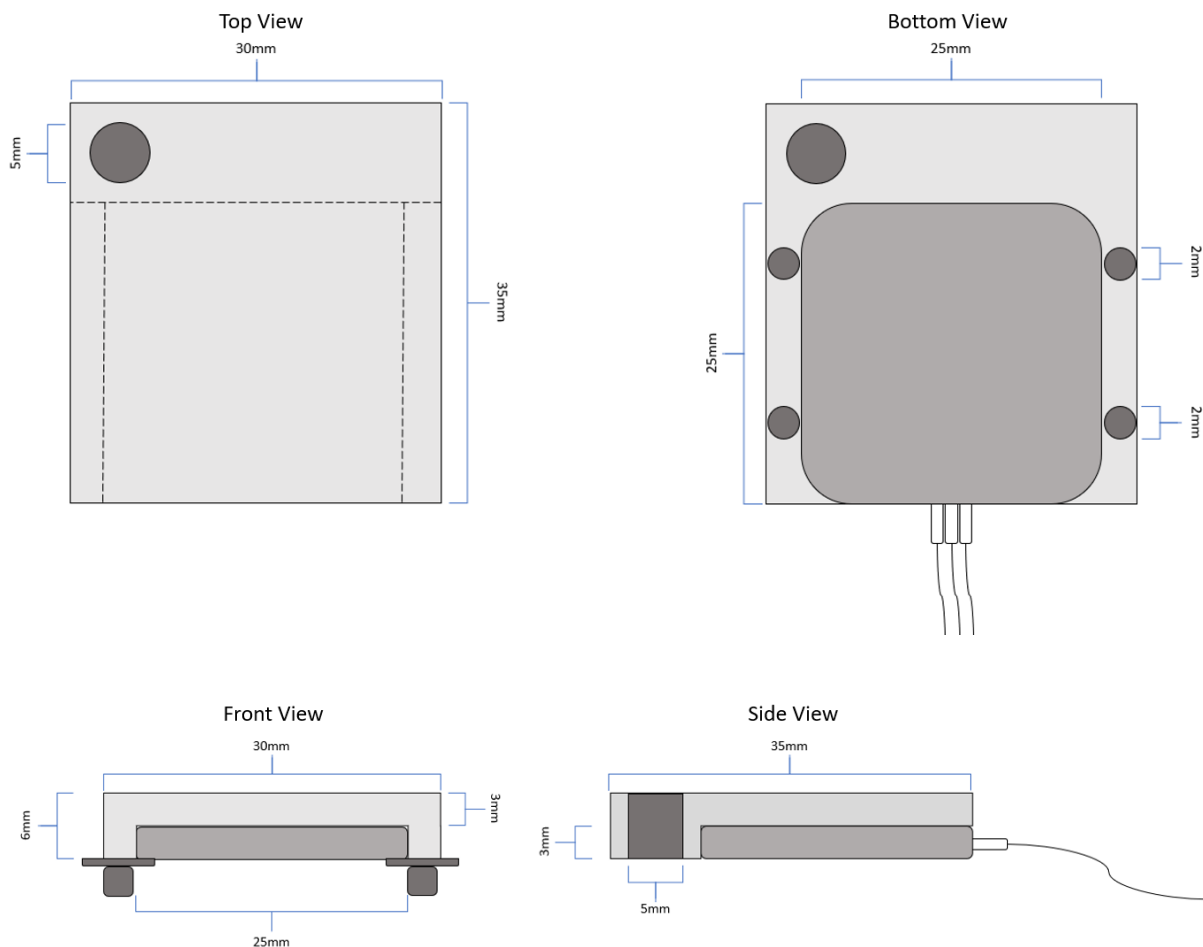
Figure 3.2 Sample stub holder and heating stage schematics

3.3 Chamber, lines, and precursor heating

Due to the high degree of control and short pulse times necessary for ALD, three Swagelok solenoid ALD valves are used to control the flow of the precursor, co-reactant and purge gas. As can be seen from Figure 3.3, two inlet pipes on the top of the chamber allow for a precursor and co-reactant line to be connected to the system. Figure 3.3 shows a schematic of these lines. The ALD lines are comprised of ¼" Swagelok stainless steel piping, while

vapour-draw ampoules are used for both the precursor and co-reactant bottles, and Swagelok vacuum fittings were used for all connections, in order to help prevent air contamination within the lines used. These lines, up to the ALD valves, are kept open to the chamber, in order for the lines to be kept under vacuum, further ensuring no air contamination in the lines and keeping the pressure in the delivery lines low, improving the vapour draw during the dose of the process chemicals. Manual shut off valves are placed at the end of each line in order to isolate the lines from the chamber, if necessary. The inert gas 'purge' line was also attached to the end of the co-reactant line, to clean the line and chamber of any unwanted reactants.
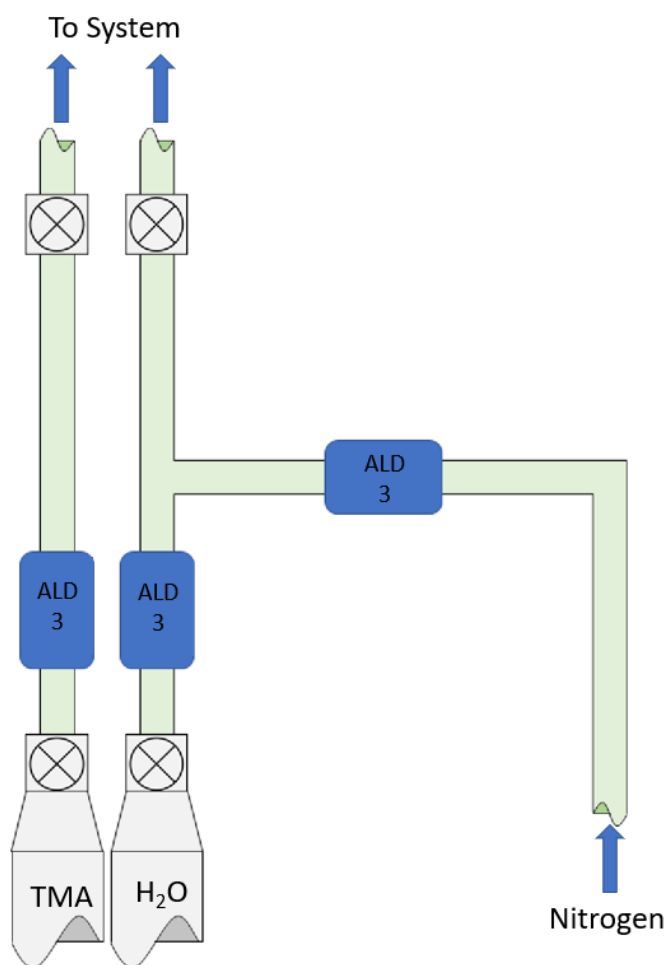

Figure 3.3 Precursor, co-reactant, and purge chamber piping schematic

These lines, along with the walls of the chamber, need to be maintained at an elevated temperature in order to prevent condensation of the precursor or co-reactant along the lines, as well as to prevent unwanted reactions along the chamber walls due to condensation within the chamber. As these temperatures do not affect the mechanics of the film growth, and do not need to be as precisely maintained, a less robust heating method was appropriate. The lines and chamber were wrapped with heating tapes with connected thermocouples, and the temperature controlled via PID temperature controller boxes, accurate to a few degrees.

3.4 ALD Valves and Calibration

3.4.1 How ALD Valves Work

The ALD valves used for this system were Swagelok ALD-3 valves, fitted with 24V electronic solenoid pilot valves. These ALD valves use a pneumatic actuator to control a normally-closed cobalt-based superalloy diaphragm. Compressed air is fed into the attached solenoid valve but is blocked from the outlet port by a 'diaphragm' held in place by a spring with a low spring constant. This diaphragm has a small pinhole, which ensures the solenoid valve's upper chamber has the same pressure as the compressed air line. When the solenoid valve is in its 'closed' position, the armature of the solenoid is pushed forward, covering the 'vent' line of the solenoid's upper chamber. When an electrical current is applied to the solenoid, the coil creates a magnetic field, which causes the armature inside the valve to retract, uncovering the upper chamber's 'vent' line. This causes the air in the upper chamber to escape, leading to a pressure reduction in the upper chamber. This pressure reduction allows the compressed air in the lower chamber to lift the diaphragm, which causes

compressed air to flow through the solenoid, into the ALD valve. This compressed air then enters the ALD valve's pneumatic actuator. This influx of compressed air causes the actuator to retract, as the pressure contracts the spring within the ALD valve's upper chamber. This, in turn, opens the diaphragm valve, allowing the gas to flow through the valve. Once the compressed air stops flowing into the ALD valve, a vent in the side of the valve allows the compressed to escape, causing the spring within the valve's pneumatic actuator to force the diaphragm closed. These ALD diaphragm valves allow for the very precise control over pulse times necessary for ALD processes, while the attached solenoids allow them to be controlled electronically. Figure 3.4 shows a schematic of this solenoid/ALD valve system in both the closed and open positions.

Closed

Compressed Air

Diaphragm

Electrical
Control

Solenoid
Magnet

Diaphragm

Precursor

To Chamber

Open

Compressed Air

Diaphragm

Electrical
Control

Solenoid
Magnet

Diaphragm

Precursor

To Chamber
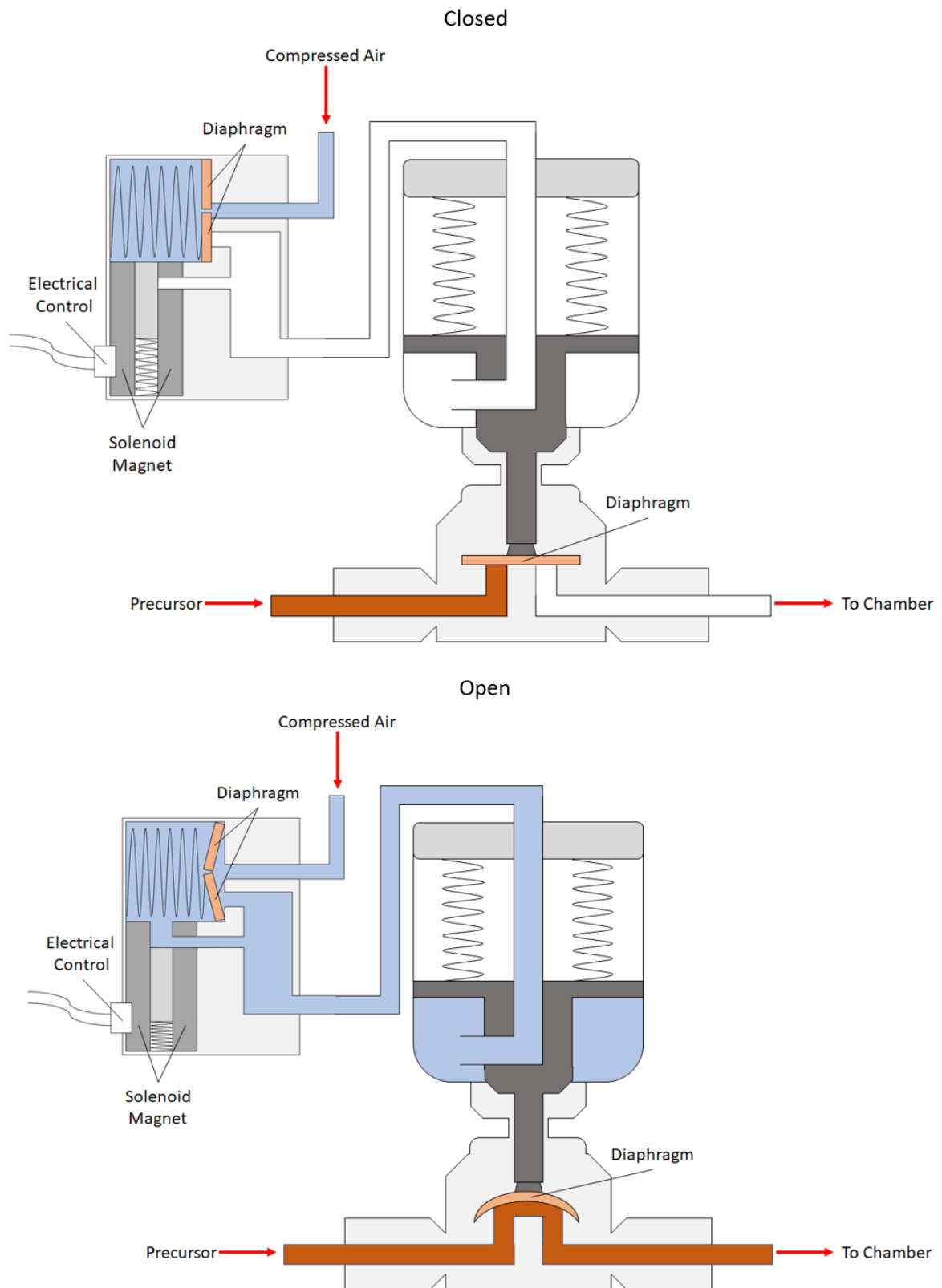
Figure 3.4 ALD valve with solenoid activation open and closed position schematic

3.4.2 Calibration and System Limitations

The ALD-3 valves used are equipped with an optical sensor which monitors the state of the ALD valve. When a sufficient voltage is supplied, the optical sensor will return this voltage while the ALD valve is in the 'open' position. The rising and falling edges of this output signal were used as an estimate for the response time of the ALD valves. Figure 3.5 shows the response curve of the ALD valve, alongside the command pulse sent by the Arduino used to electronically control the valves.
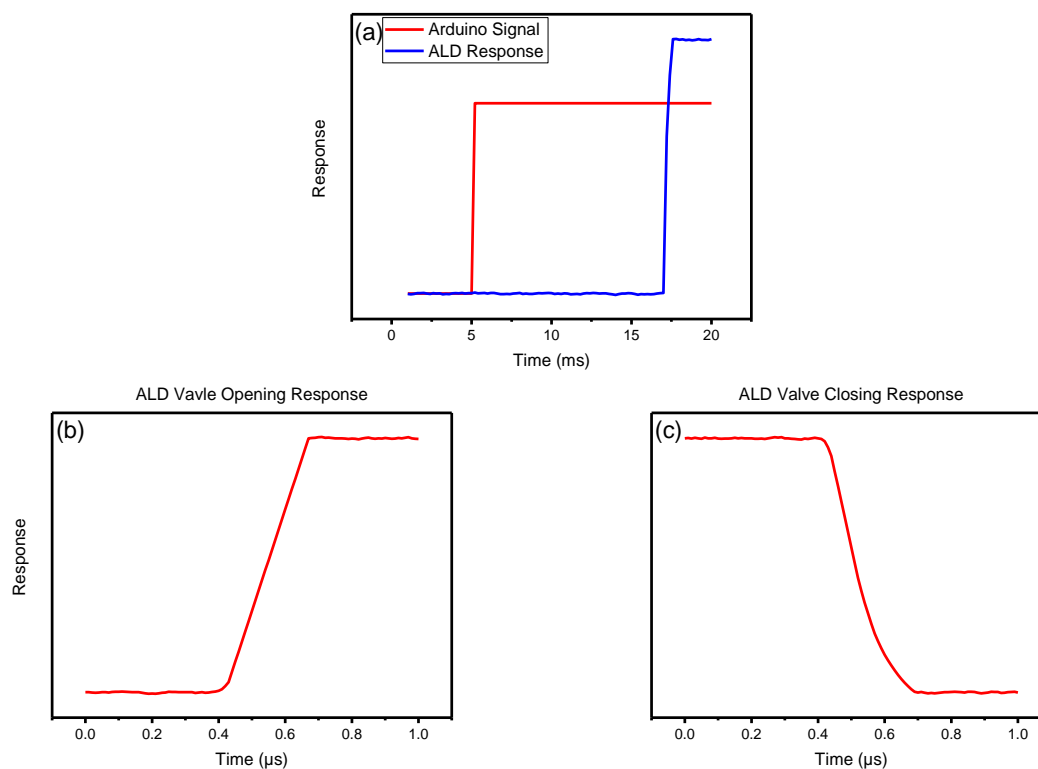
Figure 3.5 (a) ALD opening response curve compared with Arduino signal, (b) ALD valve

opening response curve, (c) ALD valve closing response curve

As shown in Figure 3.5, while the delay between the command signal and valve state, 12ms, may be noticeable, with respect to the time scale of the system, the response time of the

ALD valves, the rising and falling edge of which are on the µs scale, are short enough to be irrelevant to the system's performance. The delay seen between the control signal output and the ALD valve's response is most likely due to a delay in the response seen by the solenoid valve activation, as the pressure in the upper chamber of the solenoid valve will not 'instantaneously' change when the vent line is covered/uncovered. While in the 'open' position, the diaphragm will not open until the pressure is the upper chamber is low enough to allow the difference in pressure between the two chambers to push the diaphragm open. Similarly, in the 'close' position, the pressure in the two chambers may take time to become equalised, before the diaphragm valve closes.

The Arduino system's response time, however, may be a limiting factor of the minimum response time of the ALD system. The Arduino's output response time was found to be on the millisecond scale, and the system was incapable of sending control signal of less than ≈10ms. Fortunately, pulse times shorter than this are generally not required for vapour-draw ALD systems, and so the process should not be affected.

3.5 Electronics and Arduino Code

An Arduino Uno was used for control of both the ALD sample stage temperature, and the ALD valves' pulse times. An Arduino was chosen for this purpose due to its accessibility, variety of applications, and the stability of its response times. A difficulty encountered while using the Arduino for this purpose, however, was that the Arduino's output pins can only output a maximum of 5V. Due to the ALD-3 valves' solenoids requirement for a 24V supply to activate, a voltage relay was needed to ensure a high enough voltage could be used to open the ALD valves, while also being controlled by the Arduino software. This relay,

powered by a separate 24V power supply, was activated by the 5V Arduino output, sending

the 24V signal to the solenoid and activating the valve, as seen in Figure 3.6.

An Arduino PID code was used to control the temperature of the sample stage. As a 40V

power supply was necessary to ensure the stage could reach high temperatures, a 5V

activated transistor was used to allow the Arduino's output to control the sample heating.

The PID code recorded the temperature of the sample stage, and applied 5V to the

transistor when the temperature dropped too low, activating the transistor and allowing the

40V power supply to reach the ceramic heater, causing the temperature to increase. Once

the stage reached the desired temperature, the Arduino's output signal would cease,

deactivating the transistor and cutting off the power to the ceramic heater. A schematic of

this circuit can be seen in Figure 3.6, along with the ALD relay driver.

The Arduino code used to control this process can be found in Appendix A
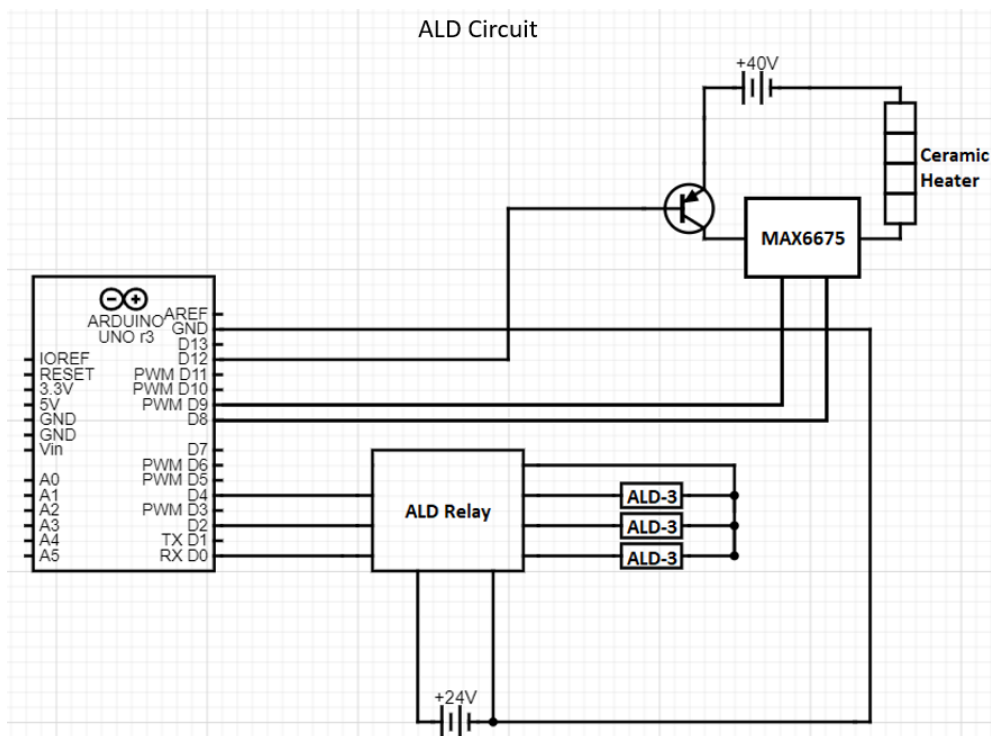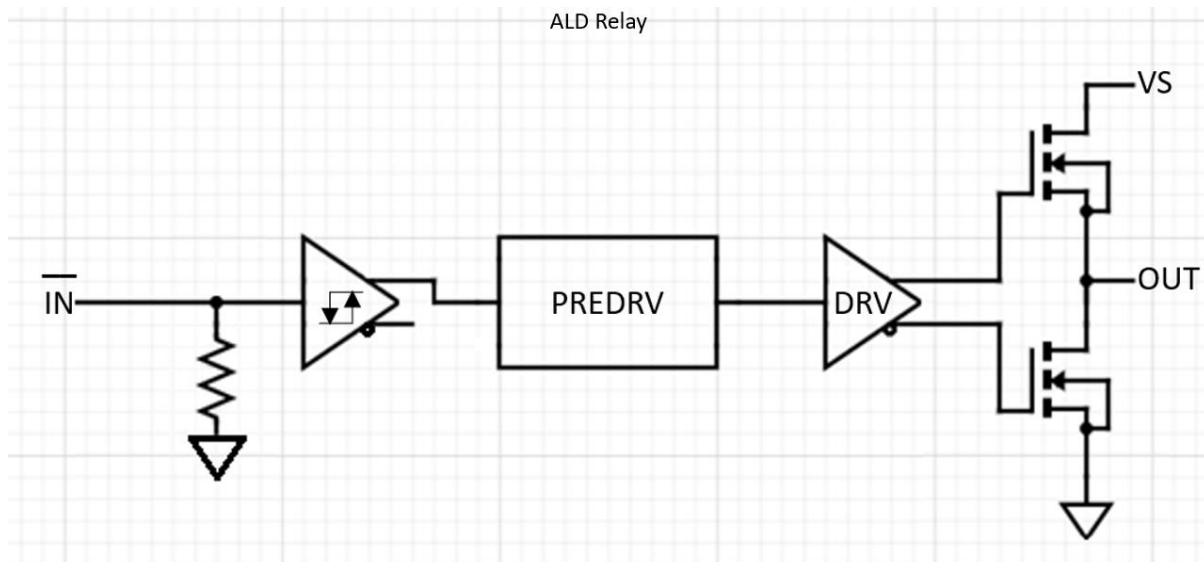
Figure 3.6 ALD heating and valve activation Arduino wiring schematic

4 ALD of Al_2O_3

4.1 Al_2O_3 Chemical Process

As discussed in section 2 above, the TMA-H_2O Al_2O_3 process was chosen as the initial recipe for this system due its wide variety of applications in the semiconductor and beyond, as well as being a relatively well understood ALD process. The interactions of the TMA and H_2O during film growth have also been documented in many studies (44,45). Figure 4.1 shows the chemical makeup of the TMA molecule.
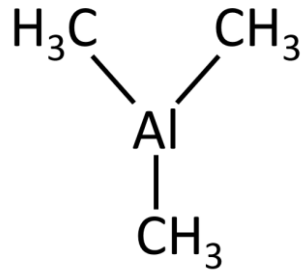
Figure 4.1 Trimethylaluminium (TMA) molecule

When this molecule interacts with an -OH terminated surface, an approximation of the chemical reaction can be seen in Equation (2.2). An idealised version of this process is also seen in Figure 4.2, where each 'half-step' of the film growth is represented. The first of these steps shows the influx of TMA during the TMA pulse. This molecule begins to interact with the -OH terminated surface. When the reaction begins, many of the bonded CH_3 molecules bond with the hydrogen on the surface, creating methane gas (CH_4). For the remaining Al-CH_3 bonds, the aluminium bonds with the surface oxygen, creating an O-Al-CH_3 bond, leaving a CH_3 surface on the substrate. An inert gas is then pumped through the system in order to 'purge' the chamber of any excess, unreacted TMA molecules, as well as removing any CH_4 biproducts from the system. Once this purge is completed, the H_2O co-reactant is pulsed into the chamber. Again, one of the hydrogen atoms in this molecule interacts with the CH_3 surface, creating the CH_4 biproduct, while the remaining OH reacts with the Al in the film, creating the Al_2O_3 film and leaving and -OH surface, ready to begin the start of the next cycle (44).
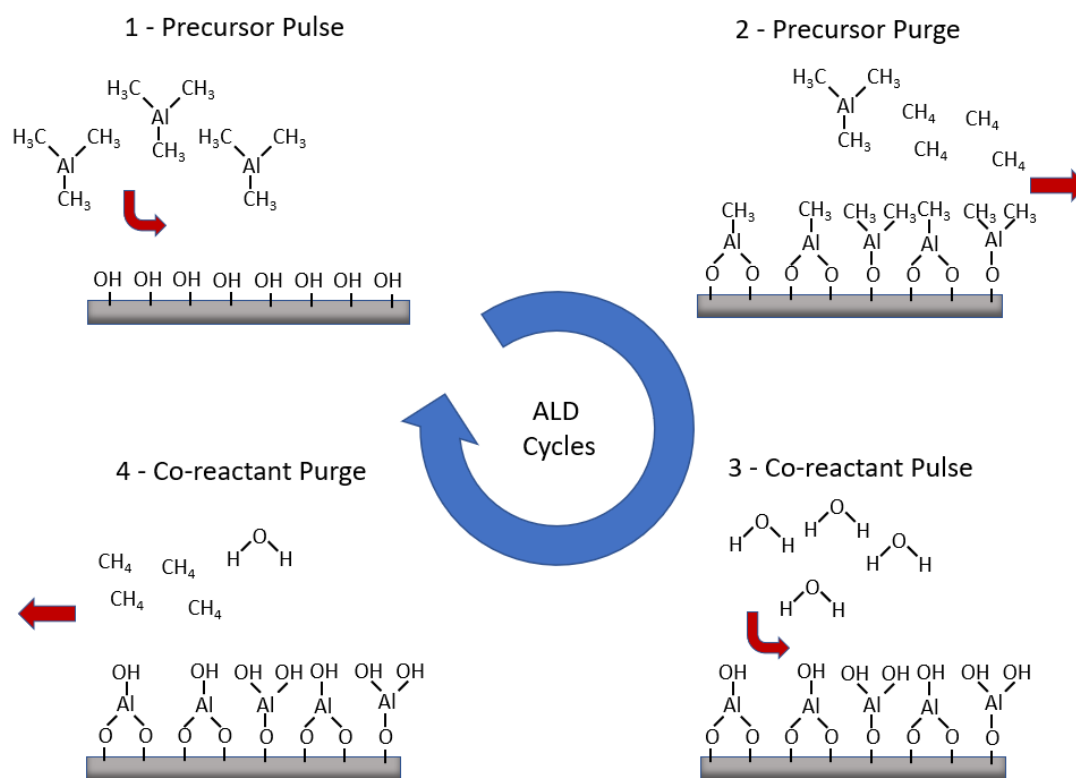
Figure 4.2 TMA-H₂O thermal ALD chemical process steps

4.2 Process Details

In this work, p-type (100) silicon was chosen as the starting substrate. XPS was used to analyse the Si sample after 1, 2, 5, 10, 20, 50 and 100 cycles of TMA and H_2O. This process was performed on native oxide Si samples heated to 150 and 250°C in order to understand the role that substrate temperature plays in the surface chemistry, and on a HF treated Si sample (5% HF solution for 15 minutes) heated at 150°C in order to examine the nucleation on pristine silicon substrates and understand how the presence of oxygen in samples with the native silicon oxide present affects the nucleation and growth. All processes were commenced with a reactor base pressure of $5x10^{-3}$ mbar. The aperture times used for the precursor dosing were 80 ms for trimethylaluminum (TMA) and 80 ms for the oxidizing co-reactant H_2O, as well as a 10 s nitrogen purge time in between each precursor and co-

reactant pulse, with the precursor and co-reactant temperatures at 40°C and room temperature, respectively.

Each TMA and H_2O pulse increased the pressure in the reactor to 3×10^{-1} and 9×10^{-2} mbar, respectively. Peak fitting was performed using AAnalyzer, implementing Voigt functions (46). EDX mapping was also performed, using a Hitachi S5500 Field Emission scanning electron microscope (SEM) in order to study the elemental distribution through thicker films.

4.3 Al_2O_3 Process Characterisation

As detailed above, the ALD growth was carried out in a sequential fashion where the number of cycles deposited on the same sample was progressively increased, with the sample undergoing XPS analysis in between the deposition steps. Figure 4.3 shows the high-resolution XPS spectra of the film growth from 1-100 cycles for the HF treated Si sample. Spectra for the HF treated sample are presented as it was the 'cleanest' of the three samples (as expected), showing the least initial oxygen. This allowed the oxygen signals to be attributed entirely to the growth process originating from H_2O and discount the possibility of dissociation of the native SiO_2 providing oxygen to the surface chemical reactions. Figure 4.3(a) shows the evolution of the Si*2p* and Al*2p* peaks for increasing cycle numbers. Note that even after one cycle evidence of aluminium on the surface can be seen, despite its relatively low photo-ionization cross section. The suppression of the bulk silicon signal with increasing cycles, seen at a binding energy of 99.4 eV is observed as expected when an overlayer is deposited, although the suppression appears to be more pronounced than one would expect for typically reported growth rates of 0.1 nm per cycle (47). The

increase in the number of ALD cycles also results in a progressive shift to higher binding energy of the Si$2p$ peak associated with oxidation of the silicon substrate and the formation of aluminium silicates (48). This suggests a strong interaction between the precursors and silicon substrate. Notably, we still observe a Si$2p$ signal even after 100 cycles (where one would expect a film of approximately 10 nm in thickness), which indicates that there appears to be some diffusion of silicon from the substrate into the aluminium oxide film. The silicon concentration is of the order of 5% (49). Other works using SIMS to examine ALD deposited Al_2O_3 films on silicon have shown similar results but not remarked on the silicon signal (50). Figure 4.3(b) shows the fitted spectra of the evolution of the Si signal, taking into account the intermediate oxidation states of silicon between the bulk Si and SiO_2 (51). The intermediate oxidation states of Si^{1+}, Si^{2+} and Si^{3+} can be seen, with an obvious growth as the cycles progress. A number of stoichiometries of aluminium silicate are thermodynamically stable and it is beyond the scope of this work to identify which are present in our films. Typically, Al-silicate has a lower dielectric constant than Al_2O_3 and as such, methods to overcome the incorporation of silicon into thin ALD films could be an important step in maximising the k-value of the resulting films.

Figure 4.3(c) shows the evolution of the O1s signal (initial binding energy, 531 eV) which can also be seen to shift to higher binding energies in later cycles. This shift to higher binding energy of the O$1s$ maximum is correlated with the growth of the Al_2O_3 film (and a small contribution from Al silicates), as the contribution from the metal oxide peak will have a higher binding energy than that of the O1s signal, causing the peak to 'shift' as more metal oxide is formed in the sample. The carbon evolution shown in Figure 4.3(d) is also observed to agree with the above area data, with the C$1s$ signal increasing in intensity, before being suppressed after later cycles due to the growth of the aluminium oxide film. This increase in

intensity is attributed to the creation carbon-aluminium bonds arising in the initial stages of growth due to incomplete surface reactions, where the CH_3 groups on the TMA molecule are not effectively removed. The binding energy position is slightly lower than that for adventitious carbon, consistent with that of metal-carbon bonds (52). However, at higher cycle numbers, this carbon-aluminium bonding stops, and the C*1s* signal can be seen to decrease as the surface carbon signal is suppressed by the aluminium oxide signal. As the cycle number increases, the carbon remaining in the film becomes oxidized, as evidenced by the shift to higher binding energy.
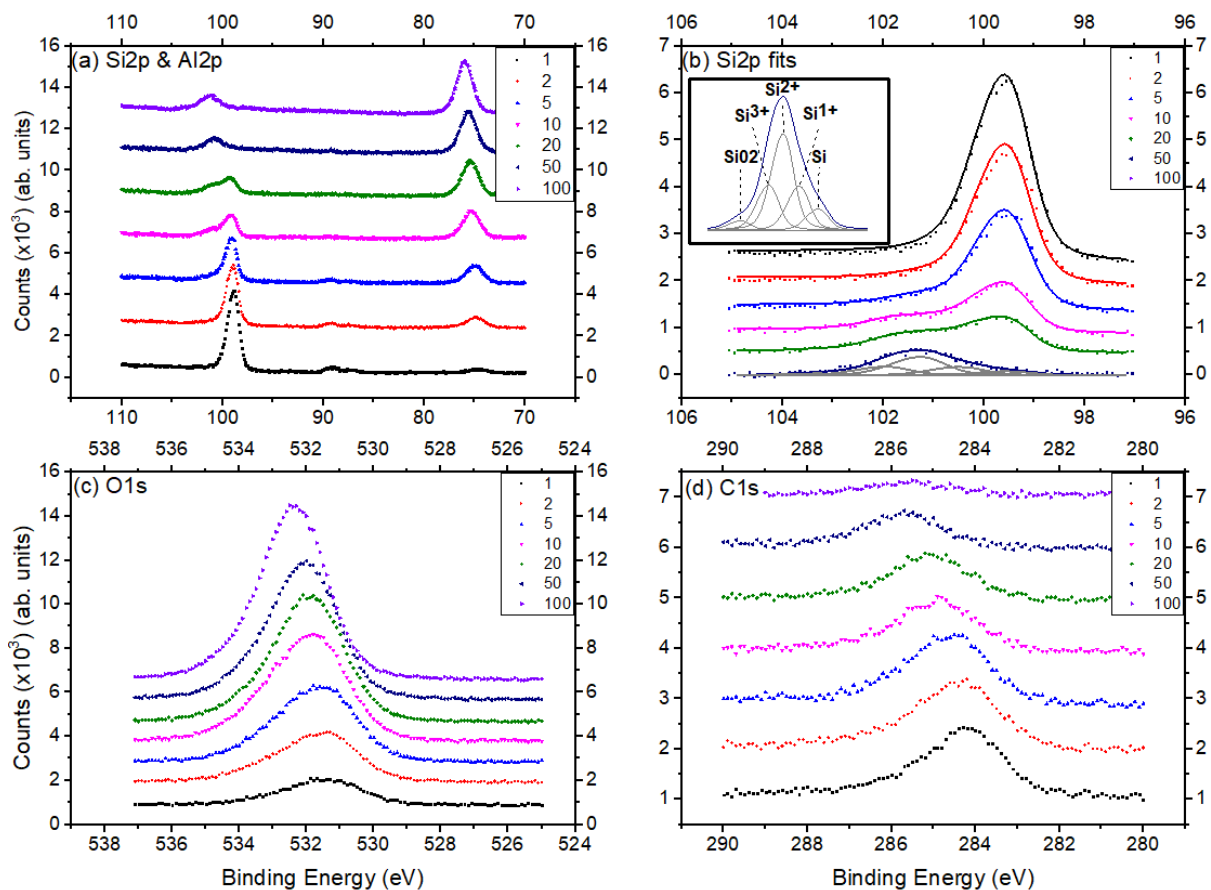
Figure 4.3 High resolution XPS spectra of the film growth from 1-100 cycles on native oxide Si, with a substrate temperature of 150°C for: (a) Si2p and Al2p peaks, (b) fitted spectra for the Si and SiO$_2$ signal evolution, with an inset showing the intermediate oxidation states of the Si peak, (c) O1s peak, (d) C1s peak.

Figure 4.4 shows a 60° off-angle XPS spectrum of a sample, compared with a spectrum acquired at normal incidence for the Si*2p*/Al*2p* region. Angle resolved XPS provides more surface sensitive information and comparison of peak profiles at normal emission and with those taken at different take off angles can give an idea of the surface localisation of elements present in the sample (53). The spectra in Figure 4.4 shows a similar profile both at normal emission and at 60° off angle, indicating that the aluminium and silicon are distributed uniformly throughout the film.
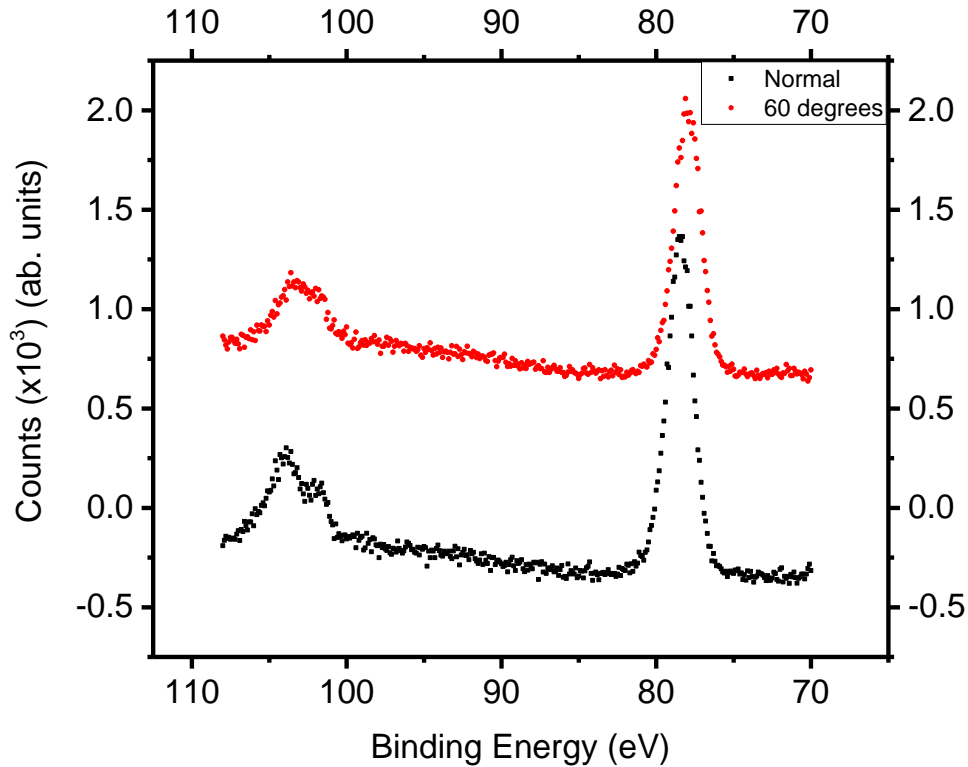
Figure 4.4 Normal and 60° off angle spectra of the Si2p and Al2p peaks

Figure 4.5 shows the peak area of the core levels for each element detected during XPS as a function of cycle number and compared for each of the samples (150°C, 250°C, 150°C HF treated). In each case the areas are normalised to the signal from the underlying silicon substrate.

Figure 4.5(a) compares the total peak areas of each of the intermediate oxidation states, or sub-oxides, between Si and SiO2 for each sample, normalised to the bulk silicon signal. The sub-oxide fits were completed using the binding energy positions outlined by Himpsel et al (51). The intermediate oxidation states can be seen to grow at with increasing cycle number. This rise in sub oxides is attributed to the significant interaction of the ALD precursors with the substrate layer, resulting in Al silicate growth (50) . The increase is

linked with the diminishing Si signal, due to continued growth of the aluminium oxide with cycles, which is suppressing the bulk signal.

Figure 4.5(b) shows the O*1s* peak intensity for each sample, again normalised to the silicon bulk. This plot shows a slightly lower concentration of oxygen in the HF treated sample in the initial stages, due to the removal of the SiO2 layer by the Hf treatment, leading to a cleaner bare Si sample. By the time 10 cycles have been deposited, an increased oxygen content is observed for the HF treated sample, indicating increased Al oxide growth, while the 250°C and 150°C sample remain indistinguishable. However, beyond 10 cycles, a rapid increase in oxygen content is observed for the 250°C sample, indicating that the higher temperature process has a significant contribution to a higher growth rate per cycle once early-stage precursor-interface surface interactions have saturated.

The behaviour observed in Figure 4.5(b) is mirrored in Figure 4.5(c), which shows the Al*2p* peak intensity for each sample as a function of the number of cycles, also normalised to the silicon bulk. The HF-treated sample facilitates a higher initial growth rate of Al oxide, with the signal growth beginning to slow towards the later cycles. The higher temperature of the substrate for the 250°C sample again appears to result in a higher growth rate beyond 10 cycles. Once the substrate-interface interactions have saturated and bulk effects begin to dominate, both the native and HF treated Si display a similar growth rate, which is to be expected as they are kept at the same temperature. Each of these plots show a larger relative peak area for the 250°C sample, indicating that the 250°C sample has the highest film growth rate of the three in the early stages. This higher growth rate is most likely due to incomplete surface reactions at the lower temperature (54).

Figure 4.5(d) shows the intensity of the C*1s* peak in each sample, normalized to the total Si signal. The intensity is seen to rise through the first ~10 cycles for each sample. Secondary ion mass spectroscopy (SIMS) work by Gosset et al. observed a similar phenomenon, which is attributed to carbon from the TMA reacting at the surface, with the initial monolayers of the deposited oxide layer containing a high concentration of unreacted methyl groups (55). This reaction is limited to the Si − Al oxide interface, with the continued growth of the aluminium oxide layer resulting in the decreasing intensity of carbon at >20 cycles. The raw area of the C*1s* peak begins to decrease for increasing numbers of cycles (not shown) in the HF treated and 250°C samples as is already observed for the 150°C sample after just 20 cycles.

In order to further understand the interactions of the TMA molecules with the surface, we investigated the ratio of carbon present at the surface solely from TMA, to the aluminium signal Figure 4.5(e). This was achieved by subtracting the initial adventitious carbon signal from the total carbon signal following each deposition and gives an idea of the extent to which methyl groups are removed from the TMA molecules during the surface reaction. In the early stages of growth, it is clear that reaction is incomplete, particularly for the samples where the native oxide is present. For example, at 250°C the ratio is approaching 3:1 indicating that most TMA molecules at the surface are fully intact, perhaps only present on the surface through physisorbtion. The situation is quickly resolved however and by the time 20 cycles are reached, we see complete removal of all carbon from the TMA as it facilitates aluminium oxide growth.
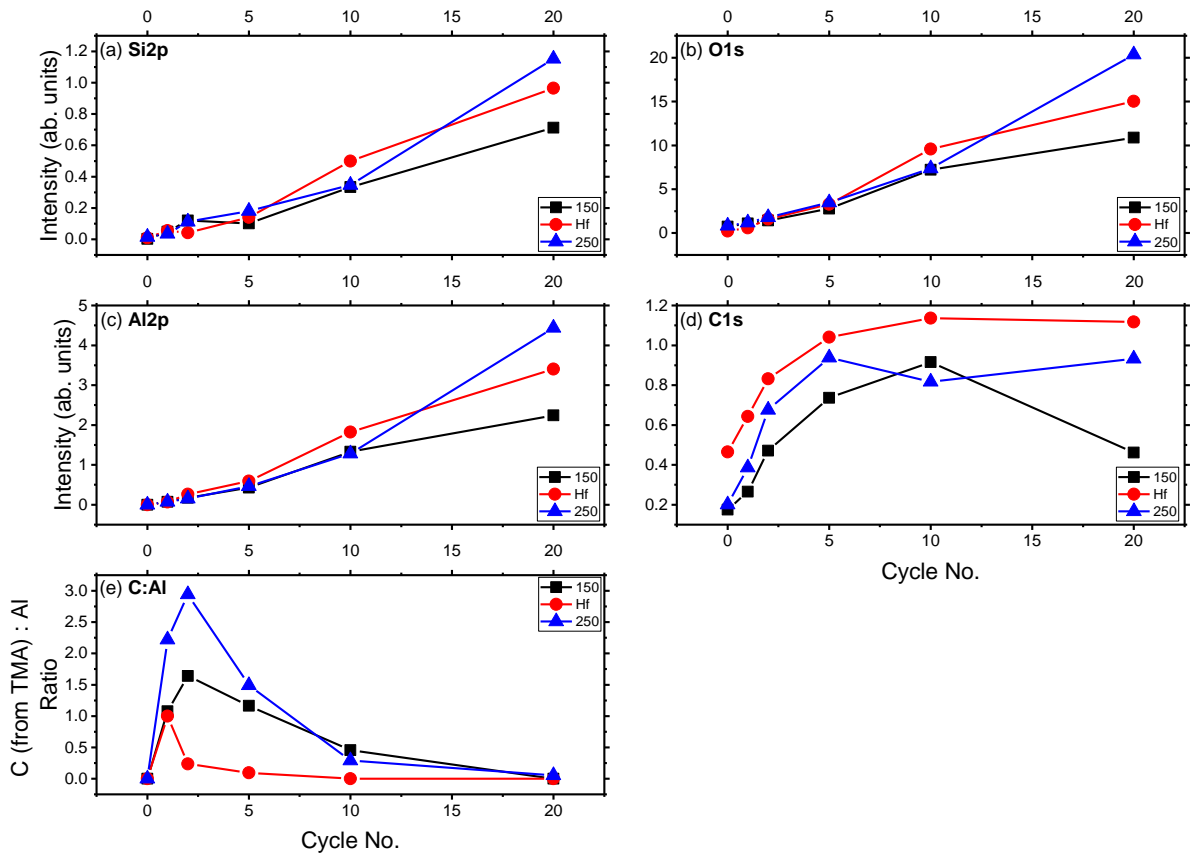
Figure 4.5 Peak area of the core levels as a function of the number of cycles for: (a) sum of the intermediate oxidation state, or sub-oxide, areas, normalised to the silicon bulk (b) O1s, normalised to the silicon bulk, (c) Al2p, normalised to the silicon bulk, (d) C1s, normalised to the silicon bulk, (e) ratio of carbon present at the surface attributed to TMA, to the aluminium signal

In order to understand the stoichiometry of the Al-oxide film grown, the respective peak areas of the aluminium and oxygen signals in the aluminium-oxide layer is shown in Figure 4.6, plotted against cycle number, up to 100 cycles. Figure 4.6(a) shows the intensity of the peak component attributed to Al-oxide growth in both the Al*2p* and O*1s* spectra, adjusted for the relative sensitivity factor of the core level, for each deposition step and indicates that in the early stages of growth there is less oxygen present than one would expect in a

stoichiometric Al_2O_3 film, consistent with the observation that Al remains bonded to carbon during the first few cycles. Figure 4.6(b) shows the ratio of Al:O in the film as the growth proceeds. Ultimately after 100 cycles we see the ratio approaching 60:40 at higher cycle numbers, which is to be expected for a stoichiometric Al_2O_3 layer.

The ratio in the initial stages of growth again clearly indicates that the film is Al rich and the oxygen deficiency correlates with the increased carbon content in the early cycles. This is coupled with a much higher growth rate in the initial stages (56). Figure 4.6(c) shows the growth in thickness of the Al_xO_y layer at each cycle number deduced from XPS overlayer intensity calculations using the method described by Kim, et al (57). Again, the film can be seen to have an extremely high initial growth rate (4 nm after 5 cycles) indicating there is significant interaction with the surface causing the suppression of the bulk silicon signal. When compared with the results for the Si$2p$ spectra discussed earlier, it appears that there is consumption of some bulk silicon which we have shown diffuses even through relatively thick films. This process, coupled with the retention of carbon from the TMA in the first few cycles, results in a very high measured growth rate when using the bulk silicon as the reference point. However, after about 20 cycles we see a constant lower growth when the ideal ALD process takes over, the carbon concentration reduces, and the Al:O ratio approaches the expect value. An average growth rate of 0.96Å per cycle can be seen for the sample, in line with the observations of other authors (49,58).
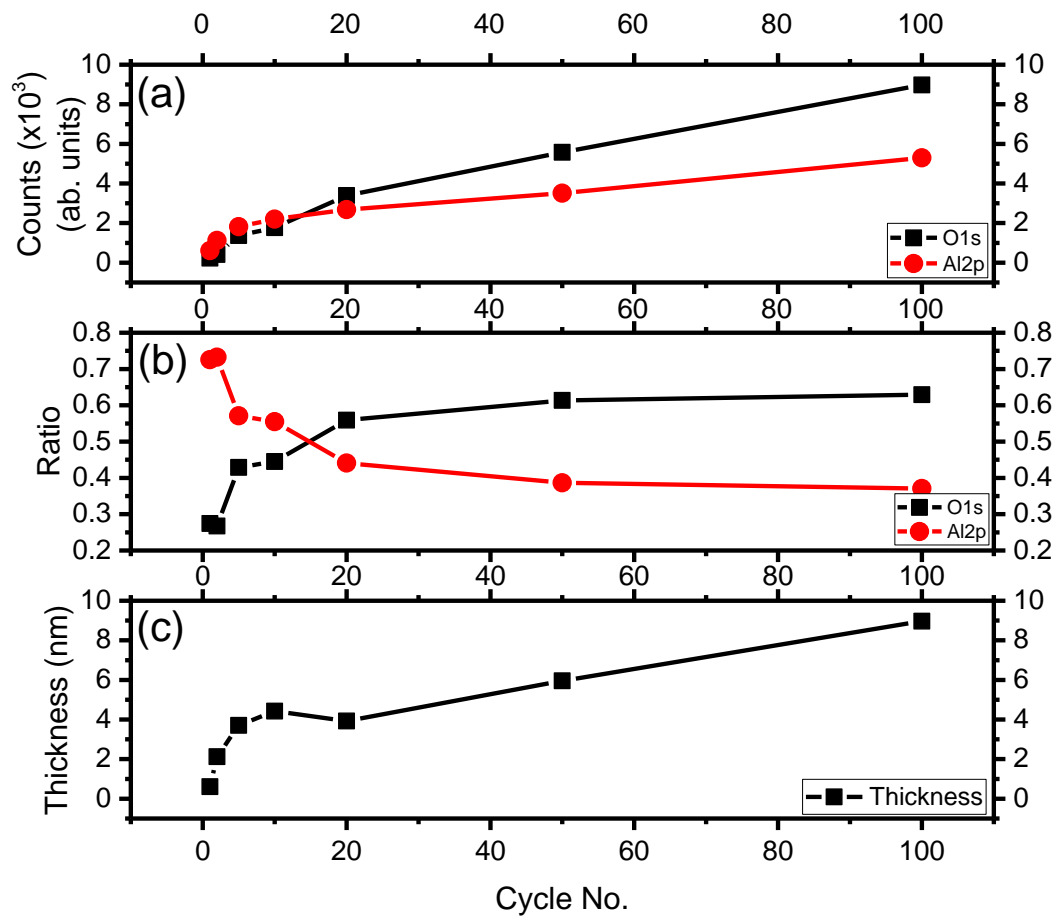
Figure 4.6 (a) Al2p and Si2p peak intensity contributed to Al-oxide growth, adjusted for their respective relative sensitivity factor, (b) Al:O ratio in the film plotted against cycle number, (c) Al_xO_y layer thickness plotted against cycle number

As XPS is sensitive to only the first few atomic layers, in order to confirm the elemental distributions suggested by XPS results in thicker films, EDX mapping was employed to measure the distribution of the elemental signals through a 200 nm thick Al_2O_3 layer grown on native oxide sSi, with a process substrate temperature of 150°C. Figure 4.7(a) clearly shows of a thin, ~15 nm, SiO_x layer on top of the silicon substrate, with the Al-oxide film on top and O and Al uniformly distributed throughout as expected (Figure 4.7(b) and (c)

respectively). Figure 4.7(d) shows the silicon EDX map, and it can be noted that silicon is also evenly distributed throughout the Al_xO_y film, more evidence of continuous silicate growth and the upward diffusion of silicon from the substrate even through several hundred ALD cycles.
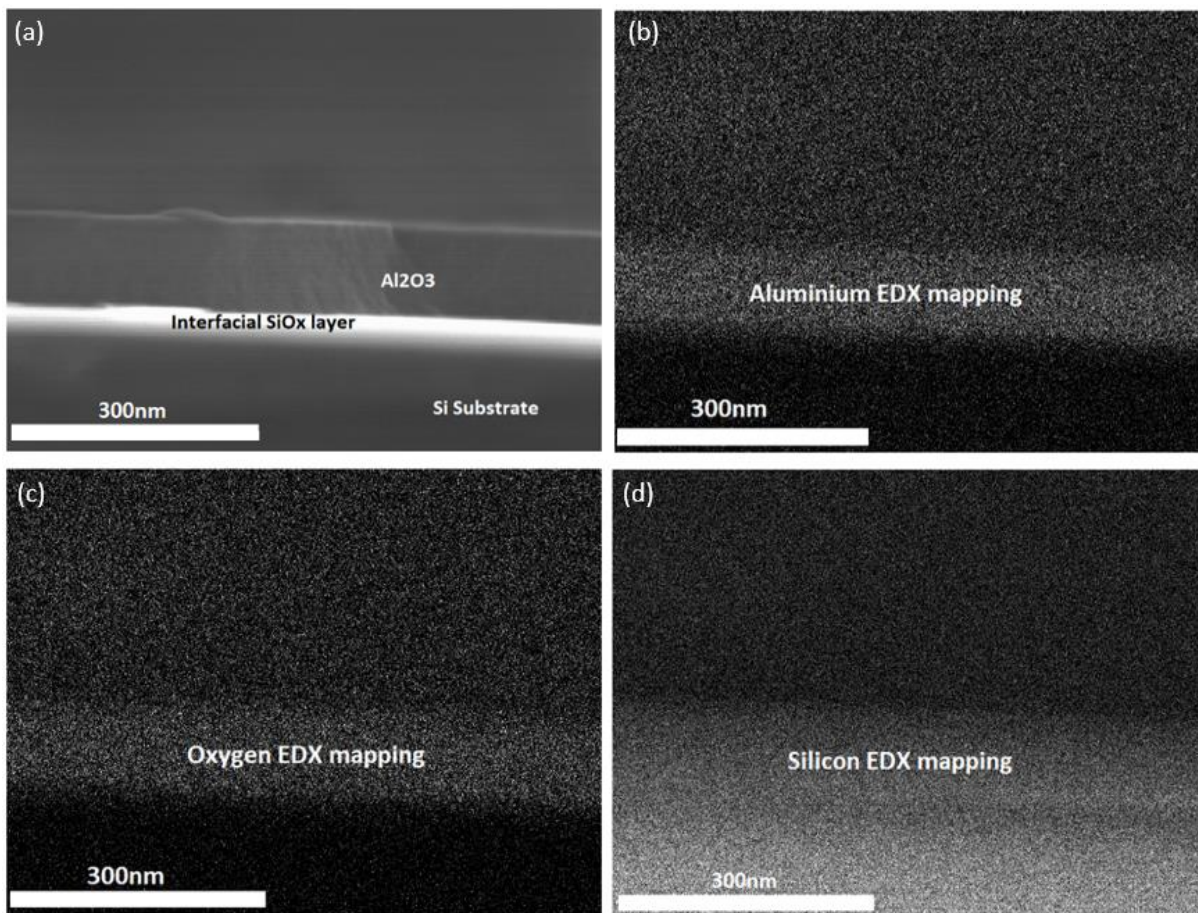

Figure 4.7 (a) EDX mapping of a thick Al_xO_y film, (b) aluminium EDX mapping of the film, (c) oxygen EDX mapping of the film, (d) silicon EDX mapping of the film

4.4 Al$_2$O$_3$ Conclusions

As can be seen from the above data, the lower sample temperature leads to a lower initial growth rate for the Al$_x$O$_y$ films during the initial stages of growth. This is most likely attributed to the lower surface temperature leading to incomplete surface reactions along the Si surface, as explained above. As shown in Figure 4.5, while the growth rate for the 250°C sample is higher than the 150°C samples, Figure 4.5(e) clearly shows less carbon contamination in the early stages of the film on the Hf treated sample. While Figure 4.6 clearly shows a varying of film composition and a lower growth rate during the initial stages of the growth rate, even of this cleaner sample, this is most likely due to the creation of an interfacial SiO$_x$ layer, which has been seen in other studies (59). EDX mapping for the films show that an interfacial layer of SiO$_x$ is created before the Al$_x$O$_y$ film growth begins. However, as shown in Figure 4.6, in the latter stages of the film growth, the growth rate per cycle comes in line with the values accepted in other works, as well as the Al$2p$ and O$1s$ ratios coming closer to the 2:3 expected in and Al$_2$O$_3$ film.

Along with the creation of an interfacial layer during the initial stages of the film growth, all films also exhibit growth of aluminosilicates, which (as shown by the EDX mapping) are distributed evenly throughout the films. While this aluminosilicate growth is observed during the early stages of growth by other authors (50,60) it is present in the films shown here up to 100 cycles. The growth of silicates in these films is most likely due to the lack of carrier gas used for the TMA and H$_2$O respectively, possibly due to the overexposure of the surface to the precursor and co-reactant during the early stages of the film growth.

5 ALD of TiO$_2$

5.1 TiO$_2$ Chemical Process

TiO$_2$ was chosen for the latter half of this work due to the stability of the films produced, as well as the robustness of the recipes used, and its variety of applications in photocatalysis, semi-conductor fabrication and beyond. The use of TTIP and H$_2$O in the growing of TiO$_2$ films has also been well documented (61,62). Figure 5.1 below shows the chemical makeup of the TTIP molecule.
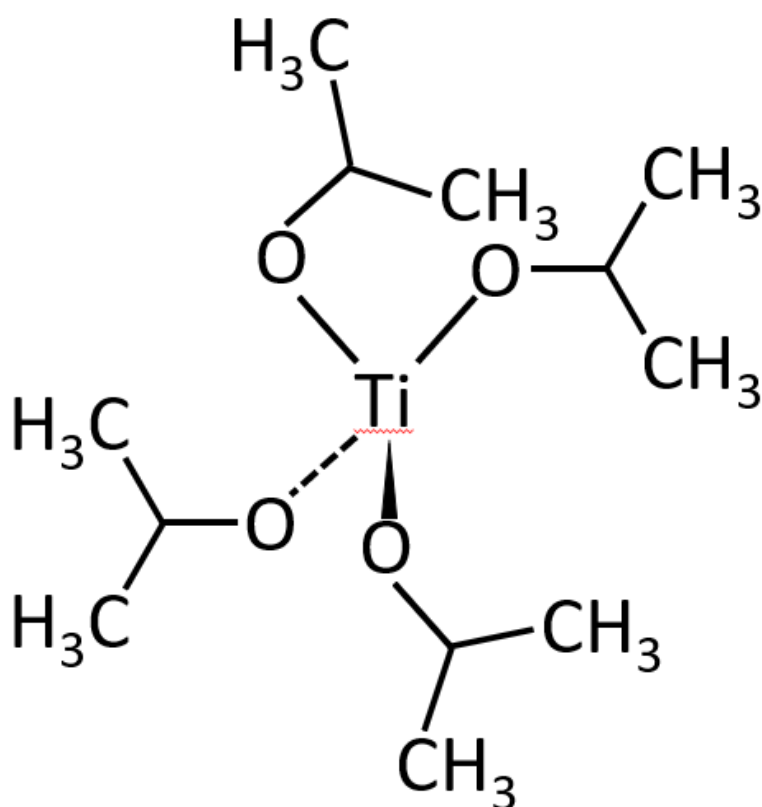

Figure 5.1 Titanium tetraisopropoxide (TTIP) molecule

As shown in Figure 5.2, the first 'half-step' of each cycle is begun when the TTIP molecule is introduced to the -OH terminated surface. When the precursor begins to react with the

surface, an intermediate step of Ti{OCH(CH$_3$)$_2$}$_3$ is created, with (CH$_3$)$_2$OHCH created as a biproduct. This excess biproduct is then flushed from the chamber during the subsequent 'purge' step, which also removes any unreacted TTIP. Once this is completed, the co-reactant is pulsed into the system. This H$_2$O co-reactant serves to react with the Ti{OCH(CH$_3$)$_2$}$_3$ surface, again creating more (CH$_3$)$_2$OHCH biproduct, and creating a new -OH terminated surface. This process is then repeated until the desired thickness of the film is achieved (28).
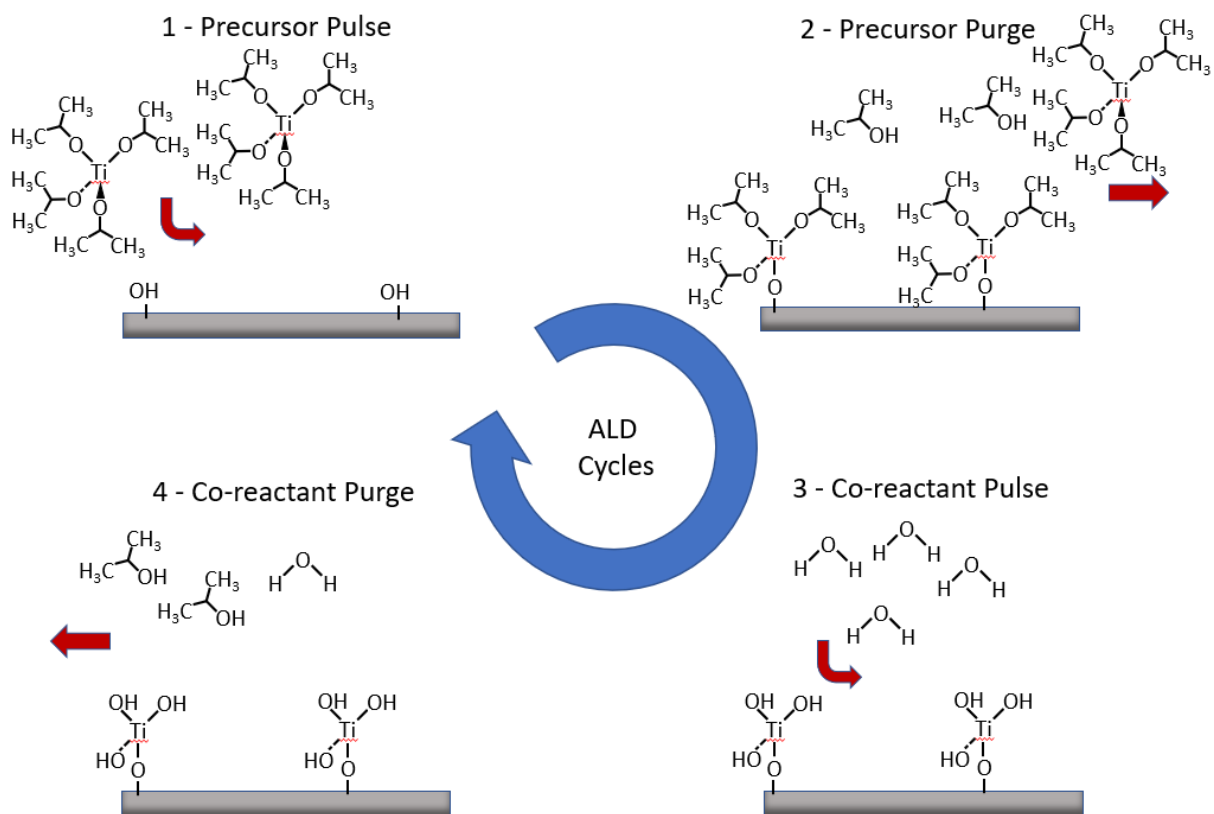

Figure 5.2 TTIP-H$_2$O thermal ALD chemical process steps

5.2 Process Details

P-type (100) silicon with resistivity of 5-9 Ω-cm was again chosen as the starting substrate for this work. While a similar process was implemented for the growth of both Al$_2$O$_3$ and

TiO$_2$, some differences in the recipes were needed in order to obtain the best films for both processes. The aperture times used for the precursor and co-reactant for the recipe used for the TiO$_2$ films were 1.5s for TTIP, and 0.2s for H$_2$O, with an inert nitrogen gas purge time of 6s used between each 'half-step'. The samples for this recipe were heated to 150°C, and XPS was employed at 10,25,50,75,100, and 300 cycles. The process was commenced at 5x10^{-3} mbar, with the pressure increasing to ~1.5mbar and ~2mbar for the precursor and co-reactant respectively.

Peak fitting was again performed using AAnalyzer, implementing Voigt functions.

5.3 TiO$_2$ Process Analysis

As explained above, a similar ALD process to the one used for the Al$_2$O$_3$ film growth was completed in order to grow TiO$_2$ thin-films. This process was carried out in a sequential, step-wise manner, where the number of cycles of film growth was progressively increased, with XPS employed for surface analysis in between these steps in order to characterise the film growth at a variety of stages. Figure 5.3 shows high-resolution spectra showing the evolution of different elements of the TiO$_2$ film growth from 10-300 cycles at 150°C.

Figure 5.3(a) shows the evolution of the Si$2p$ peak as the cycle number increases. The bulk Si$2p$ signal can be clearly seen to be suppressed as the cycles number increases, with no Si signal can be seen after 150 cycles, and only a small amount being visible after 100 cycles. This Si suppression implies a growth rate of ~0.9Å per cycle, which is in-line with other such studies (63,64). During the early stages of film growth, some oxidation states of the Si$2p$ peak can be seen, which are attributed to the native oxide on the surface of the substrate.

However, after 50 cycles, this SiO_2 signal is almost completely suppressed by the TiO_2 film growth, showing that no silicates growth is observed for this process. Figure 5.3(b) shows a similar evolution for the Ti$2p^{3/2}$ and Ti$2p^{1/2}$ signals. Note that due to Ti's relatively low photo-ionization cross section after 10 cycles the Ti$2p$ signal is only barely visible. The position of the Ti$2p$ peaks at 458.5 eV and 464.5 eV respectively show that the entirety of the Ti$2p$ signal can be attributed to TiO_2, with no Ti metal signal (usually seen at 454.1 eV and 461.1 eV) visible at any stage during the film growth.

Figure 5.3(c) shows the O$1s$ component of the film growth. Like the Ti$2p$ evolution, the amount of oxygen in the film can be clearly seen to increase with higher cycle numbers. The majority of the O$1s$ signal for this film can also be seen to shift dramatically from its position at 531 eV during the initial stages (which is associated with oxygen in the native silicon oxide on the surface of the sample) to a lower binding energy of 529.3 eV as more and more of the oxygen in the surface of the sample is associated with oxygen within the titanium oxide film than with the native oxide. After 150 cycles, almost all of the O$1s$ signal shown is at this lower binding energy, implying that all of the oxygen present was due to the substrate's surface oxide prior to the beginning of the film growth. At 300 cycles, a peak at high binding energy can once again be seen, which is most likely due to the adsorption of water vapour to the surface, as the sample was sitting in vacuum for an extended periods of time before being scanned for a final time.

Finally, Figure 5.3(d) shows the C$1s$ signal at each cycle number. These spectra show an increase in the intensity of the carbon signal during the earlier cycles before the signal is supressed in the later cycles. This signal suppression is due to less carbon being incorporated into the film at later growth stages, and the signal associated with the surface

and initial cycles' carbon being suppressed by the peaks associated with the TiO$_2$ growth. Similarly to during the Al$_2$O$_3$ process, this increase in carbon during the earlier stages of the film growth is attributed to carbon bonds within the film during the earlier growth stages due to incomplete surface reactions, where the CH$_3$ groups from the TTIP precursor are not removed effectively and some carbon in incorporated into the film. However, some carbon is seen to be incorporated throughout the entirety of the film, likely due to incomplete surface reactions, and film contamination within the chamber. At 300 cycles, an increase in the carbon signal is again observed, particularly at high binding energy, which is associated with C-O and C=O bonds. As with the *O1s* peak, this can be attributed to the sample sitting in vacuum before being scanned.
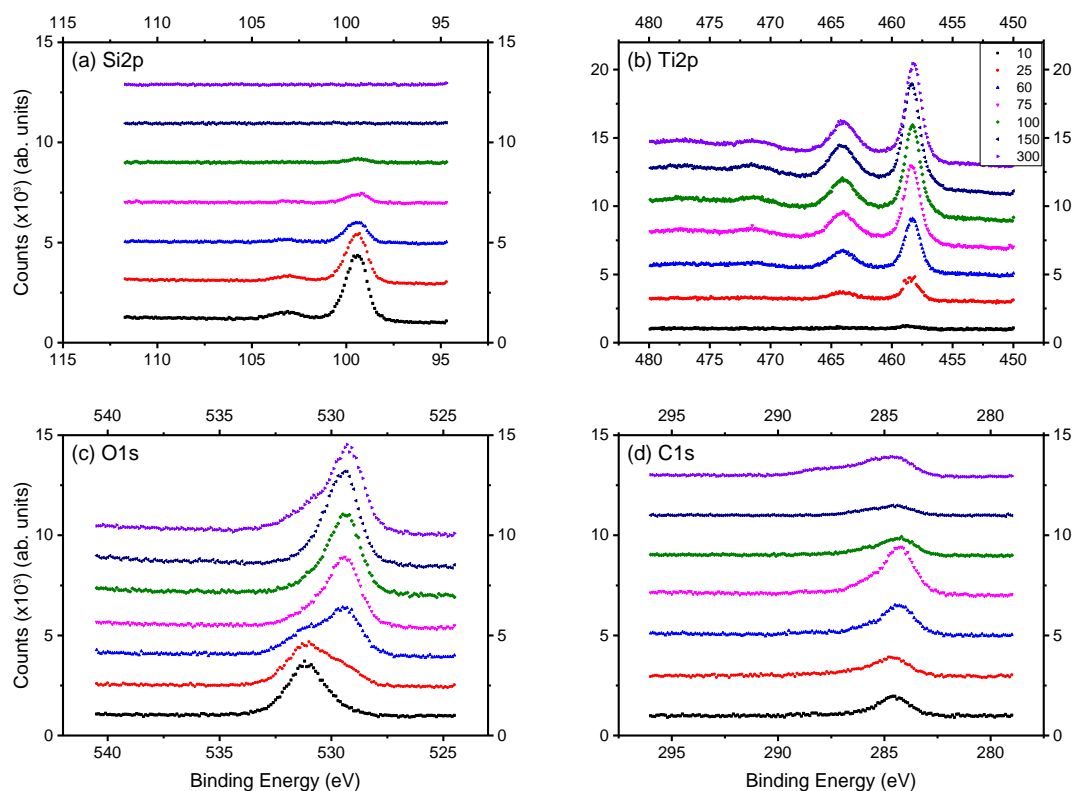
*Figure 5.3 High resolution XPS spectra of the film growth from 10-300 cycles for: (a) the Si2p peak, (b) Ti2p$^{3/2}$ and Ti2p$^{1/2}$ peaks, (c) the O1s peak, (d) the C1s peak, on a native oxide Si substrate*

Figure 5.4 shows the thickness of the TiO_2 film plotted against the cycle number. These thicknesses were calculated using the "Thickogram" XPS thickness calculation outlined by Cumpson, et al (65). The "Thickogram" uses a graphical method to compare the intensity of the substrate and overlayer, taking the binding energy and R.S.F of both into account to estimate the thickness of grown films from XPS spectra. From these thickness calculations, it is obvious that the growth rate of the TiO_2 films is much more stable than that of the Al_2O_3 films grown during this work, with much les dependence on an interfacial layer during the initial growth stages. This is in line with the findings of other such studies, showing a much more uniform growth rate per cycle during the initial growth stages (27). No thickness calculations are shown above 100 cycles, as the "Thickogram" method of thickness calculations can only be used with XPS spectra when both the film and substrate are clearly visible. As XPS can only penetrate the first ~10 nm of a substance, films thicker than this cannot be measured using XPS analysis. The average growth rate associated with this process is 0.88Å, which is well within the literature values associated with similar thermal TTIP processes (63,64). Further future work may involve an analysis of the initial stages of growth of a similar TiO_2 film grown using TTIP in order to ascertain the growth mode during the very early stages (<10 cycles) of film growth.
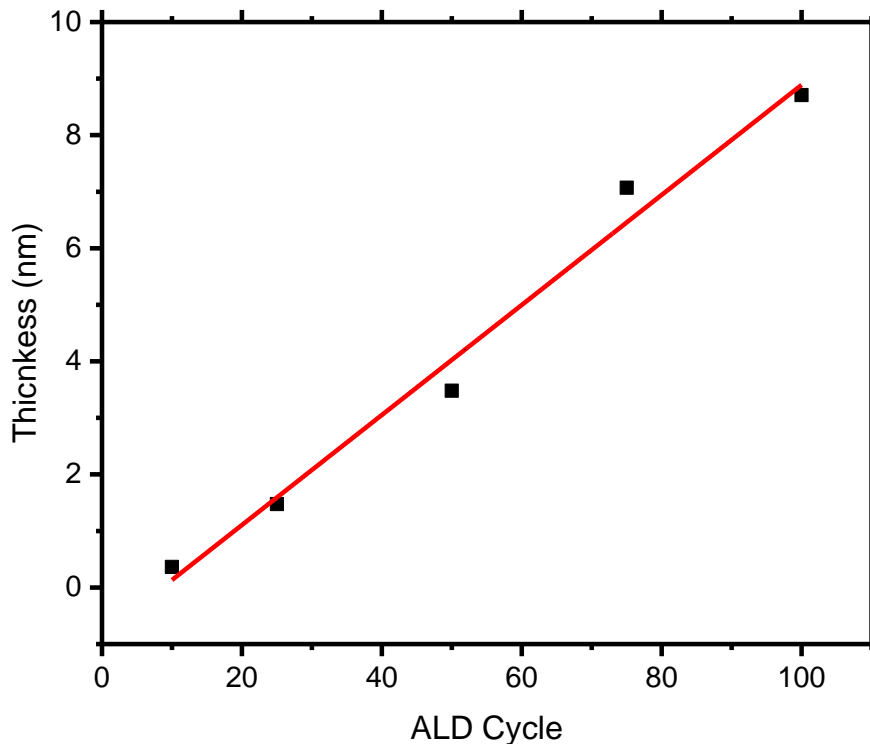
Figure 5.4 TiO$_2$ film thickness plotted against cycle number from 10-100 cycles

Finally, Figure 5.5 shows the percentage composition of the TiO$_2$ films. Figure 5.5(a) shows the percentage composition of the sample's surface at varying cycle numbers from 10-300. Here, the carbon increase during the initial stages of the growth can be clearly seen, before it begins to be supressed after 100 cycles. The percentage composition of both oxygen and titanium can also be seen to stabilise in the latter stages of the film growth. However, even in the earlier stages of the growth, the ratio of both elements can be seen to be much more stable than during the Al$_2$O$_3$ process.

Figure 5.5(b) shows the percentage composition of TiO$_2$ films grown using similar processes as different substrate temperatures. The 100°C shows a slightly lower percentage of oxygen in the final film, most likely due to incomplete reactions caused by the insufficient heat energy needed to drive interactions at the lower temperature. The carbon percentage in each of the films is also seen to decrease slightly as the temperature of the substrate

increases. This is attributed to the increased temperature ensuring a more ideal film growth, having sufficient energy to allow the surface reactions to be completed.
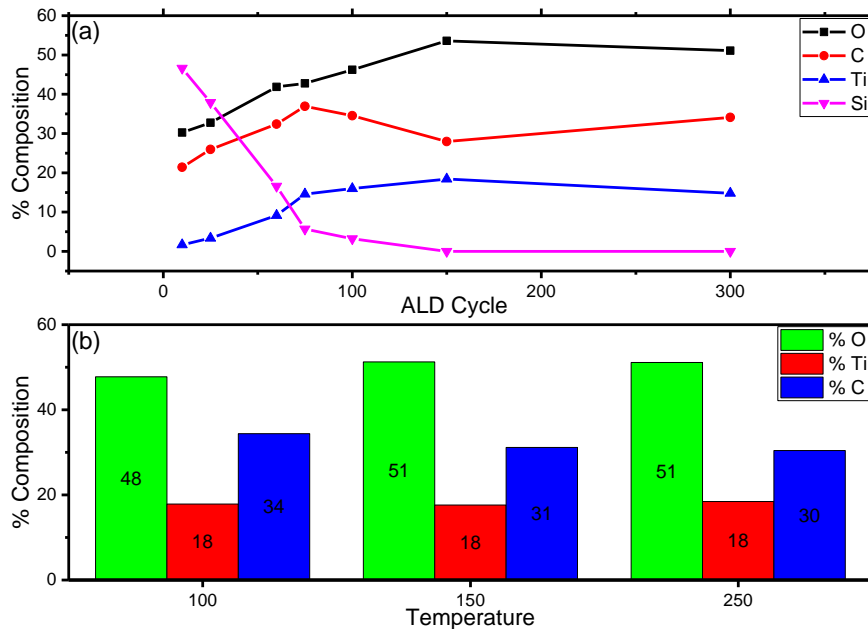
Figure 5.5 Percentage composition of the TiO$_2$ films: (a) from 10-300 cycles, (b) of a thick, 20 nm film grown at 100, 150, and 250 degrees

5.4 TiO$_2$ Conclusions

As shown in the above data, while the TiO$_2$ films grown do exhibit some non-ideal growth during the early cycles, similar to the Al$_x$O$_y$ films, growth stabilisation is observed much earlier during the growth cycle for TiO$_2$ films. As shown in Figure 5.3(d), during the early stages, some excess carbon is observed in the films, most likely due to incomplete surface reactions during the initial growth stages, leading to some CH$_3$ groups from the TTIP precursor not being successfully purged from the film. From Figure 5.3(a), the growth of the TiO$_2$ film can be seen to entirely suppress the Si signal after 150 cycles. This suppression shows that no silicates were grown during the TiO$_2$ deposition cycles, giving a cleaner film than the Al$_x$O$_y$ counterpart.

Figure 5.3(b) shows the evolution Ti$2p$ signal as the deposition cycle number increases. The positions of the Ti$2p^{3/2}$ and Ti$2p^{1/2}$ peaks, at 458.5 eV and 464.5 eV respectively, show that during the growth cycles, all of the Ti incorporated into the grown film is converted to TiO$_2$, showing that the surface interactions during the film growth are completed successfully during each step. Figure 5.5(b) shows the influence of different substrate temperatures on the film growth. The 100°C exhibits a slightly higher percentage of carbon in the film than those grown at a higher temperature. This is attributed to incomplete surface reactions during the deposition due to insufficient energy to correctly drive the interactions at the lower temperature.

6 Conclusions

6.1 Discussions and Conclusions

The results and work above show the workings of a 'home-built' atomic layer deposition system, coupled with an in-situ x-ray photoelectron spectroscopy analysis tool. As can be seen from the above data, the system design was implemented successfully and thermal film growth was achieved for both Al_xO_y and TiO_2 films, using both TMA and TTIP as precursors, respectively, with H_2O as a co-reactant in both cases. For both processes, the growth rates and composition of the films produced agreed with those reported by other studies growing similar films. A higher temperature for both films led to cleaner final films, which is attributed to the lower temperature processes leading to incomplete surface reactions due to insufficient energy to drive the reactions to completion.

An interfacial layer was also observed during the early stages of the films' growth, which can be seen on the EDX mapping of the Al_xO_y film. This interfacial layer growth is most likely caused by the reaction of the precursors and co-reactants with the bare Si, rather than with the surface of a grown film. However, as can be seen from the plotted growth rates of both processes, the TiO_2 process stabilises much faster than the Al_xO_y process, likely due to the creation of a much smaller interfacial layer.

Using a bubbled precursor, or attaching an inert gas line to the precursor input line may help with this interfacial layer creation, as well as preventing silicate production during the Al_xO_y process, as a constant inert gas flow during the precursor doses may help to prevent unwanted reactions with the silicon surface during the early stages of growth. Using mass flow controllers to control the flow of the inert gas used may also be useful to ensure greater control of the purge steps, and to better control the pressure within the chamber.

When compared with films grown using a commercial Oxford Plasma Technology FlexAl ALD system, the films grown over the course of this work had both a much higher carbon content and a higher growth rate per cycle. The higher carbon contents seen in the films grown using the 'home-built' ALD system outlined in this work is attributed to a higher system base pressure during depositions. This higher pressure is due to it being necessary to isolate the turbo pump during depositions to prevent a build-up of precursor on the turbo blades. On the commercial FlexAl system, a specialised, heated turbo pump is employed, allowing the turbo pump to run during depositions, lowering the system's base pressure during deposition cycles.

Another reason for the higher growth rates and carbon contents of the films grown by this system may be due to a higher partial pressure during the precursor pulses. When comparing the TiO_2 processes on both systems, the partial pressure during the precursor doses when using the 'home-built' system is higher (~2mbar) than on the commercial FlexAl system (~0.4mbar). This higher partial pulse pressure leads to a much larger amount of Ti being pulsed into the system during the dose step, causing a higher growth rate per cycle.

The partial pressure difference between these two systems shows an issue with the reporting of recipes within the area of ALD research. Previous research most commonly reports only the dose times used for the precursor and co-reactant in recipes. This has a similar problem to the one described above; similar dose times across different systems can lead to varying amounts of precursor in the system during dose steps, due to different partial pressure increases caused by the precursor. This partial pressure difference can be caused by varying chamber sizes, wall and line temperatures, ampoule pressures, precursor line lengths, and a variety of other chamber variables. Using partial pressures as a method

of reporting precursor pulses is a more appropriate system, as it ensures the same amount of a precursor is interacting with the surface of a sample across a variety of systems.

6.2 Future Work

As this is, comparatively, a small study, some further research into this area in the future would be beneficial. Ideally, a wider array of precursors and co-reactants could be used in order to grow and compare a wider variety of atomic layer deposition films. Repeating these experiments at a wider range of process parameters (temperature, dose times, purge times, etc.) would also be beneficial, to help gain better understanding of the effects of changing parameters on the film growth. These films could also be compared with films grown using similar parameters in an industrial scale ALD tool, to ensure the films are of comparable quality. Comparing films grown on a system with a different geometry to the one used in this work, using similar dose times, could also be a case for further study, as it would help compare the difference reporting only dose times makes to the quality and stoichiometry of films grown across different systems.

Some of the limitations of this 'home-built' system could also be addressed in the future, including setting up a 'bubbler' line for precursors that use a bubbled ampoule, attaching more specialised, heated pumps, to prevent precursor build-up on the pump blades, and a system to help further automate the sample transfer process. A plasma system could also be attached, to allow the use of PE-ALD, allowing for a greater variety of films to be grown.

Bibliography

1. Koster G, Rijnders G, editors. Insitu Characterisation of Thin film growth. Woodhead Publishing; 2011. 296 p.

2. George SM. Atomic layer deposition: An overview. Chem Rev. 2010;110(1):111–31.

3. Malygin AA, Drozd VE, Malkov AA, Smirnov VM. From V. B. Aleskovskii's "framework" Hypothesis to the Method of Molecular Layering/Atomic Layer Deposition [Internet]. Vol. 21, Chemical Vapor Deposition. Wiley-VCH Verlag; 2015 [cited 2020 Mar 24]. p. 216–40. Available from: http://doi.wiley.com/10.1002/cvde.201502013

4. Puurunen RL. A short history of atomic layer deposition: Tuomo Suntola's atomic layer epitaxy. Chem Vap Depos [Internet]. 2014 Dec 1 [cited 2020 Mar 24];20(10–12):332–44. Available from: http://doi.wiley.com/10.1002/cvde.201402012

5. Goodman CHL, Pessa M V. Atomic layer epitaxy. J Appl Phys [Internet]. 1986 Aug 14 [cited 2020 Mar 26];60(3):R65–82. Available from: http://aip.scitation.org/doi/10.1063/1.337344

6. Johnson RW, Hultqvist A, Bent SF. A brief review of atomic layer deposition: From fundamentals to applications. Mater Today [Internet]. 2014 [cited 2019 Sep 30];17(5):236–46. Available from: https://pdf.sciencedirectassets.com/272281/1-s2.0-S1369702114X00064/1-s2.0-S1369702114001436/main.pdf?X-Amz-Security-Token=AgoJb3JpZ2luX2VjEOb%2F%2F%2F%2F%2F%2F%2F%2F%2F%2FwEaCXVzLWVhc3QtMSJHMEUCIER4F7GC%2BMpgMGogU0Xxh8l0GwPmO3BcYBwlIfUZA%2B5vAiEA90K3%2B4

7. Profijt HB, Potts SE, van de Sanden MCM, Kessels WMM. Plasma-Assisted Atomic Layer Deposition: Basics, Opportunities, and Challenges. J Vac Sci Technol A Vacuum, Surfaces, Film [Internet]. 2011 [cited 2020 Mar 30];29(5):050801. Available from: https://doi.org/10.1116/1.3609974

8. Niskanen A, Rahtu A, Sajavaara T, Arstila K, Ritala M, Leskelä M. Radical-Enhanced Atomic Layer Deposition of Metallic Copper Thin Films. J Electrochem Soc. 2005;152(1):G25.

9. Kwak JC, Lee YH, Choi BH. Preparation of tantalum oxide thin films by photo-assisted atomic layer deposition. Appl Surf Sci. 2004;230(1–4):249–53.

10. Puurunen RL. Surface chemistry of atomic layer deposition: A case study for the trimethylaluminum/water process. J Appl Phys [Internet]. 2005 Jun 15 [cited 2018 Oct 5];97(12):121301. Available from: http://aip.scitation.org/doi/10.1063/1.1940727

11. Soto C, Tysoe WT. The reaction pathway for the growth of alumina on high surface area alumina and in ultrahigh vacuum by a reaction between trimethyl aluminum and water. J Vac Sci Technol A Vacuum, Surfaces, Film [Internet]. 1991 Sep 4 [cited 2020 Mar 26];9(5):2686–95. Available from: http://avs.scitation.org/doi/10.1116/1.577226

12. Groner MD, Fabreguette FH, Elam JW, George SM. Low-Temperature Al2O3 Atomic Layer Deposition. Chem Mater [Internet]. 2004;16(4):639–45. Available from: http://pubs.acs.org/doi/abs/10.1021/cm0304546

13. Juppo M, Rahtu A, Ritala M. In situ mass spectrometry study on surface reactions in atomic layer deposition of TiN and Ti(Al)N thin films. Chem Mater [Internet]. 2002 [cited 2019 Feb 5];14(1):281–7. Available from:

https://pubs.acs.org/sharingguidelines

14. Uusitalo AM, Pakkanen TT, Kröger-Laukkanen M, Niinistö L, Hakala K, Paavola S, et al. Heterogenization of racemic ethylenebis(1-indenyl)zirconium dichloride on trimethylaluminum vapor modified silica surface [Internet]. Vol. 160, Journal of Molecular Catalysis A: Chemical. 2000 [cited 2020 Mar 26]. Available from: www.elsevier.comrlocatermolcata

15. Puurunen RL, Vandervorst W. Island growth as a growth mode in atomic layer deposition: A phenomenological model. J Appl Phys [Internet]. 2004 [cited 2020 Mar 30];96(12):7686–95. Available from: https://doi.org/10.1063/1.1810193

16. Arroval T, Aarik L, Rammula R, Kruusla V, Aarik J. Effect of substrate-enhanced and inhibited growth on atomic layer deposition and properties of aluminum-titanium oxide films. Thin Solid Films [Internet]. 2016 Feb 1 [cited 2020 Mar 30];600:119–25. Available from: https://linkinghub.elsevier.com/retrieve/pii/S0040609016000377

17. Lamagna L, Wiemer C, Perego M, Spiga S, Rodríguez J, Santiago Coll D, et al. Mechanisms for substrate-enhanced growth during the early stages of atomic layer deposition of alumina onto silicon nitride surfaces. Chem Mater. 2012 Mar 27;24(6):1080–90.

18. De Almeida RMC, Baumvol IJR. Reaction-diffusion in high-k dielectrics on Si. Surf Sci Rep. 2003;49(1–3):1–114.

19. Kim H. Atomic layer deposition of metal and nitride thin films: Current research efforts and applications for semiconductor device processing. J Vac Sci Technol B Microelectron Nanom Struct [Internet]. 2003 [cited 2020 Mar 30];21(6):2231.

Available from: https://doi.org/10.1116/1.1622676

20. De Ridder M, Van De Ven PC, Van Welzenis RG, Brongersma HH, Helfensteyn S, Creemers C, et al. Growth of iron oxide on yttria-stabilized zirconia by atomic layer deposition. J Phys Chem B [Internet]. 2002 [cited 2020 Mar 30];106(51):13146–53. Available from: https://pubs.acs.org/sharingguidelines

21. Satta Alessandra A, Schuhmacher J, Whelan CM, Vandervorst W, Brongersma SH, Beyer GP, et al. Growth mechanism and continuity of atomic layer deposited TiN films on thermal SiO2. J Appl Phys [Internet]. 2002 [cited 2020 Mar 30];92(12):7641–6. Available from: https://doi.org/10.1063/1.1522485

22. Alam MA, Green ML. Mathematical description of atomic layer deposition and its application to the nucleation and growth of HfO2 gate dielectric layers. J Appl Phys [Internet]. 2003 [cited 2020 Mar 30];94(5):3403–13. Available from: https://doi.org/10.1063/1.1599978

23. Ye PD, Yang B, Ng KK, Bude J, Wilk GD, Halder S, et al. GaN metal-oxide-semiconductor high-electron-mobility-transistor with atomic layer deposited Al2 O3 as gate dielectric. Appl Phys Lett [Internet]. 2005 [cited 2020 Mar 31];86(6):1–3. Available from: https://doi.org/10.1063/1.1861122

24. Kryder MH, Wang S, Rook K. FeAlN/SiO2 and FeAlN/Al2O3 multilayers for thin-film recording heads (invited). J Appl Phys [Internet]. 1993 May 15 [cited 2020 Mar 31];73(10):6212–7. Available from: http://aip.scitation.org/doi/10.1063/1.352702

25. Gharachorlou A, Detwiler MD, Gu XK, Mayr L, Klötzer B, Greeley J, et al. Trimethylaluminum and Oxygen Atomic Layer Deposition on Hydroxyl-Free Cu(111).

ACS Appl Mater Interfaces [Internet]. 2015 [cited 2020 Mar 31];7(30):16428–39. Available from: www.acsami.org

26.   Dingemans G, Kessels WMM. Status and prospects of Al 2 O 3 -based surface passivation schemes for silicon solar cells . J Vac Sci Technol A Vacuum, Surfaces, Film [Internet]. 2012 [cited 2020 Mar 31];30(4):040802. Available from: https://doi.org/10.1116/1.4728205

27.   Pore V, Rahtu A, Leskelä M, Ritala M, Sajavaara T, Keinonen J. Atomic layer deposition of photocatalytic TiO2 thin films from titanium tetramethoxide and water. Chem Vap Depos. 2004 Jun;10(3):143–8.

28.   Hackler RA, Kang G, Schatz GC, Stair PC, Van Duyne RP. Analysis of TiO 2 Atomic Layer Deposition Surface Chemistry and Evidence of Propene Oligomerization Using Surface-Enhanced Raman Spectroscopy. J Am Chem Soc. 2019 Jan 9;141(1):414–22.

29.   Chaukulkar RP, Agarwal S. Atomic layer deposition of titanium dioxide using titanium tetrachloride and titanium tetraisopropoxide as precursors. J Vac Sci Technol A Vacuum, Surfaces, Film [Internet]. 2013 May [cited 2020 Nov 18];31(3):031509. Available from: http://avs.scitation.org/doi/10.1116/1.4798385

30.   Lee SY, Jeon C, Kim SH, Kim Y, Jung W, An KS, et al. In-situ X-ray photoemission spectroscopy study of atomic layer deposition of TiO 2 on silicon substrate. Jpn J Appl Phys [Internet]. 2012 Mar 29 [cited 2020 Nov 18];51(3 PART 1):031102. Available from: https://iopscience.iop.org/article/10.1143/JJAP.51.031102

31.   Wang Y, Sun C, Zhao X, Cui B, Zeng Z, Wang A, et al. The Application of Nano-TiO2 Photo Semiconductors in Agriculture [Internet]. Vol. 11, Nanoscale Research Letters.

Springer New York LLC; 2016 [cited 2020 Nov 19]. Available from:

/pmc/articles/PMC5126030/?report=abstract

32. Kurtoglu ME, Longenbach T, Gogotsi Y. Preventing Sodium Poisoning of Photocatalytic

TiO2 Films on Glass by Metal Doping. Int J Appl Glas Sci [Internet]. 2011 Jun [cited

2020 Nov 19];2(2):108–16. Available from: http://doi.wiley.com/10.1111/j.2041-

1294.2011.00040.x

33. Ziental D, Czarczynska-Goslinska B, Mlynarczyk DT, Glowacka-Sobotta A, Stanisz B,

Goslinski T, et al. Titanium dioxide nanoparticles: Prospects and applications in

medicine [Internet]. Vol. 10, Nanomaterials. MDPI AG; 2020 [cited 2020 Nov 19].

Available from: /pmc/articles/PMC7075317/?report=abstract

34. Mogilevsky G, Chen Q, Kleinhammes A, Wu Y. The structure of multilayered titania

nanotubes based on delaminated anatase. Chem Phys Lett. 2008 Jul 30;460(4–

6):517–20.

35. Sharma J, Beard BC. Fundamentals of X-ray Photoelectron Spectroscopy(XPS) and Its

Applications to Explosives and Propellants. In: Chemistry and Physics of Energetic

Materials. Springer Netherlands; 1990. p. 569–85.

36. Tanuma S, Powell CJ, Penn DR. Calculations of electron inelastic mean free paths. IX.

Data for 41 elemental solids over the 50 eV to 30 keV range. Surf Interface Anal

[Internet]. 2011 Mar 1 [cited 2020 Mar 31];43(3):689–713. Available from:

http://doi.wiley.com/10.1002/sia.3522

37. Moulder JF, Stickle WF, Sobol PE, Bomben KD. Handbook of X-ray photoelectron

spectroscopy: a reference book of standard spectra for identification and

interpretation of XPS data [Internet]. Surface and Interface Analysis. 1992 [cited 2020

Apr 29]. Available from: https://www.cnyn.unam.mx/~wencel/XPS/MANXPS.pdf

38.   Edgell MJ, Paynter RW, Castle JE. High energy xps using a monochromated Ag Lα

source: resolution, sensitivity and photoelectric cross sections. J Electron Spectros

Relat Phenomena [Internet]. 1985 Jan [cited 2020 Apr 22];37(2):241–56. Available

from: https://linkinghub.elsevier.com/retrieve/pii/0368204885800712

39.   Christie A. Methods of Surface Analysis. Methods of Surface Analysis. Elsevier; 1975.

152–153 p.

40.   Scofield JH. Hartree-Slater subshell photoionization cross-sections at 1254 and 1487

eV. J Electron Spectros Relat Phenomena [Internet]. 1976 Jan [cited 2020 Apr

1];8(2):129–37. Available from:

https://linkinghub.elsevier.com/retrieve/pii/0368204876800151

41.   Zommer L. Determination of the spectrometer transmission function for XPS

quantitative analysis. Vacuum. 1995 May 1;46(5–6):617–20.

42.   Lindgren I. Chemical shifts in X-ray and photo-electron spectroscopy: A historical

review. Vols. 137–140, Journal of Electron Spectroscopy and Related Phenomena.

2004.

43.   Greczynski G, Hultman L. X-ray photoelectron spectroscopy: Towards reliable binding

energy referencing. Vol. 107, Progress in Materials Science. Elsevier Ltd; 2020. p.

100591.

44.   Lownsbury JM, Gladden JA, Campbell CT, Kim IS, Martinson ABF. Direct

Measurements of Half-Cycle Reaction Heats during Atomic Layer Deposition by

Calorimetry. Chem Mater [Internet]. 2017 [cited 2021 Jan 19];29(20):8566–77. Available from: https://pubs.acs.org/sharingguidelines

45. Halls MD, Raghavachari K. Atomic Layer Deposition Growth Reactions of Al2O3 on Si(100)-2×1. J Phys Chem B [Internet]. 2004 Apr 1 [cited 2021 Jan 19];108(13):4058–62. Available from: https://pubs.acs.org/sharingguidelines

46. Herrera-Gomez A, Bravo-Sanchez M, Ceballos-Sanchez O, Vazquez-Lepe MO. Practical methods for background subtraction in photoemission spectra. Surf Interface Anal [Internet]. 2014 Oct 1 [cited 2019 Sep 30];46(10–11):897–905. Available from: http://doi.wiley.com/10.1002/sia.5453

47. Herrera-Gomez A, Sun Y, Aguirre-Tostado FS, Hwang C, Mani-Gonzalez PG, Flint E, et al. Structure of ultra-thin diamond-like carbon films grown with filtered cathodic arc on Si(001). Anal Sci [Internet]. 2010 Feb 10 [cited 2019 Sep 30];26(2):267–72. Available from: http://joi.jlc.jst.go.jp/JST.JSTAGE/analsci/26.267?from=CrossRef

48. Stoch J, Lercher J, Ceckiewicz S. Correlations between XPS binding energies and composition of aluminasilicate and phosphate molecular sieves. Zeolites [Internet]. 1992 Jan [cited 2019 Sep 20];12(1):81–5. Available from: https://linkinghub.elsevier.com/retrieve/pii/014424499290015H

49. Ha SC, Choi E, Kim SH, Roh JS. Influence of oxidant source on the property of atomic layer deposited Al2O3 on hydrogen-terminated Si substrate. Thin Solid Films [Internet]. 2005 Apr 8 [cited 2019 Sep 20];476(2):252–7. Available from: https://www-sciencedirect-com.dcu.idm.oclc.org/science/article/pii/S004060900401377X

50.   Klein TM, Niu D, Epling WS, Li W, Maher DM, Hobbs CC, et al. Evidence of aluminum silicate formation during chemical vapor deposition of amorphous Al2O3 thin films on Si(100). Appl Phys Lett [Internet]. 1999 [cited 2019 Aug 20];75(25):4001–3. Available from:

http://dx.doi.org/10.1063/1.125519http://scitation.aip.org/content/aip/journal/apl/75/25?ver=pdfcov

51.   Himpsel FJ, McFeely FR, Taleb-Ibrahimi A, Yarmoff JA, Hollinger G. Microscopic structure of the SiO2/Si interface. Phys Rev B [Internet]. 1988 Sep 15 [cited 2019 Sep 30];38(9):6084–96. Available from:

https://link.aps.org/doi/10.1103/PhysRevB.38.6084

52.   Kim J, Lee B, Park SY, Kim HC, Cho K, Vogel EM, et al. Conformal Al2O3 dielectric layer deposited by atomic layer deposition for graphene-based nanoelectronics. Appl Phys Lett [Internet]. 2008 May 19 [cited 2019 Sep 20];92(20):203102. Available from:

http://aip.scitation.org/doi/10.1063/1.2928228

53.   Cumpson PJ. Angle-resolved XPS and AES: Depth-resolution limits and a general comparison of properties of depth-profile reconstruction methods. J Electron Spectros Relat Phenomena. 1995 May 31;73(1):25–52.

54.   Matero R, Rahtu A, Ritala M, Leskelä M, Sajavaara T. Effect of water dose on the atomic layer deposition rate of oxide thin films. Thin Solid Films. 2000;368(1):1–7.

55.   Gosset LG, Damlencourt JF, Renault O, Rouchon D, Holliger P, Ermolieff A, et al. Interface and material characterization of thin Al2O3 layers deposited by ALD using TMA/H2O. J Non Cryst Solids [Internet]. 2002 May [cited 2019 Sep 20];303(1):17–23.

Available from: https://linkinghub.elsevier.com/retrieve/pii/S0022309302009584

56.   Klein TM, Niu D, Epling WS, Li W, Maher DM, Hobbs CC, et al. Evidence of aluminum
       silicate formation during chemical vapor deposition of amorphous Al2O3 thin films on
       Si(100). Appl Phys Lett. 1999 Dec 20;75(25):4001–3.

57.   Kim KJ, Jang JS, Lee JH, Jee YJ, Jun CS. Determination of the absolute thickness of
       ultrathin Al2O 3 overlayers on Si (100) substrate. Anal Chem. 2009 Oct
       15;81(20):8519–22.

58.   Haeberle J, Henkel K, Gargouri H, Naumann F, Gruska B, Arens M, et al. Ellipsometry
       and XPS comparative studies of thermal and plasma enhanced atomic layer deposited
       Al2O3-films. Beilstein J Nanotechnol. 2013;4(1):732–42.

59.   Gakis GP, Vahlas C, Vergnes H, Dourdain S, Tison Y, Martinez H, et al. Investigation of
       the initial deposition steps and the interfacial layer of Atomic Layer Deposited (ALD)
       Al2O3 on Si. Appl Surf Sci [Internet]. 2019 Oct 30 [cited 2020 Nov 19];492:245–54.
       Available from: https://linkinghub.elsevier.com/retrieve/pii/S0169433219319415

60.   Lale A, Scheid E, Cristiano F, Datas L, Reig B, Launay J, et al. Study of aluminium oxide
       thin films deposited by plasma-enhanced atomic layer deposition from tri-methyl-
       aluminium and dioxygen precursors: Investigation of interfacial and structural
       properties. Thin Solid Films [Internet]. 2018 [cited 2020 Nov 19];666:20–7. Available
       from: https://hal.laas.fr/hal-02043421

61.   Cho K, Park JD, Shin C. Atomic layer deposition of TiO2 using titanium isopropoxide
       and H2O: Operational principle of equipment and parameter setting. J Semicond
       Technol Sci. 2016;16(3):346–51.

62.   Chaker A, Szkutnik PD, Pointet J, Gonon P, Vallée C, Bsiesy A. Understanding the

      mechanisms of interfacial reactions during TiO2 layer growth on RuO2 by atomic

      layer deposition with O2 plasma or H2O as oxygen source. J Appl Phys [Internet].

      2016 Aug 28 [cited 2021 Jan 19];120(8):085315. Available from:

      http://aip.scitation.org/doi/10.1063/1.4960139

63.   Xie Q, Musschoot J, Deduytsche D, Van Meirhaeghe RL, Detavernier C, Van den

      Berghe S, et al. Growth Kinetics and Crystallization Behavior of TiO[sub 2] Films

      Prepared by Plasma Enhanced Atomic Layer Deposition. J Electrochem Soc [Internet].

      2008 Jul 25 [cited 2020 Nov 24];155(9):H688. Available from:

      https://iopscience.iop.org/article/10.1149/1.2955724

64.   Tallarida M, Friedrich D, Städter M, Michling M, Schmeisser D. Growth of TiO 2 with

      thermal and plasma enhanced atomic layer deposition. In: Journal of Nanoscience

      and Nanotechnology. 2011. p. 8049–53.

65.   Cumpson PJ, Zalm PC. Thickogram: A method for easy film thickness measurement in

      XPS. Surf Interface Anal [Internet]. 2000 Jun 1 [cited 2019 Sep 13];29(6):403–6.

      Available from: http://doi.wiley.com/10.1002/1096-

      9918%28200006%2929%3A6%3C403%3A%3AAID-SIA884%3E3.0.CO%3B2-8

Appendix A

ALD Code

```cpp
#include <PID_v1.h>
#include "max6675.h"
#include <stdio.h>
#include <string.h>

const int TempSet = 150;
const int TMALength = 20;
const int H2OLength = 80;
const int PurgeLength = 10000;
const int WaitTime = 10000;
const int Cycles = 10;


int ktcSO = 12;
int ktcCS = 10;
int ktcCLK = 13;

MAX6675 ktc(ktcCLK, ktcCS, ktcSO);

//output pin for heater
#define PIN_OUTPUT 3

//Define Variables
double Setpoint, Input, Output;

//Initial Parameters
double Kp = 2, Ki = 5, Kd = 1;
PID myPID(&Input, &Output, &Setpoint, Kp, Ki, Kd, DIRECT);

//////////////////////////////////////////////////

struct Valve {
  int pin;
  int valvedel;
  int pumptime;
} valve1, valve2, valve3;

Valve valves[3] = {valve1, valve2, valve3};

int buttonPin = 7;
int run;



void setup()
{
  valve1.pin = 4;
  valve2.pin = 5;
  valve3.pin = 6;

  valve1.valvedel = PurgeLength;
  valve2.valvedel = H2OLength;
  valve3.valvedel = TMALength;

  valve1.pumptime = WaitTime;
```

```arduino
  Serial.begin(9600);
  delay(500);
  //initial variables
  Setpoint = TempSet;

  //PID on
  myPID.SetMode(AUTOMATIC);


  run = 0; //starts stopped
  pinMode(buttonPin, INPUT_PULLUP);
  pinMode(valve1.pin, OUTPUT);    //Sets the pin as an output
  pinMode(valve2.pin, OUTPUT);
  pinMode(valve3.pin, OUTPUT);


}

void loop()
{

  int valvenum = 0;
  for (int i = 1; i <= Cycles; i++)
  {
    if (Input >= 0)
    {
      Serial.println("   ");
      Serial.print("Cycle no.     ");
      Serial.println(i);
      Serial.println("   ");

      ///Runs PID Controller for 7 seconds///

      int starttime = millis();
      int endtime = starttime;
      while ((endtime - starttime) <= valve1.pumptime)
      {

        Serial.println(ktc.readCelsius());
        delay(200);
        //Uses celcius read from max as input
        Input = ktc.readCelsius();
        myPID.Compute();
        analogWrite(PIN_OUTPUT, Output);
        endtime = millis();
      }

      digitalWrite(valve1.pin, HIGH);
      delay(valve1.valvedel);
      digitalWrite(valve1.pin, LOW);

      ////////Runs PID heater////////////////////

      starttime = millis();
      endtime = starttime;
      while ((endtime - starttime) <= valve1.pumptime)
      {
        Serial.println(ktc.readCelsius());
        delay(200);
        //Uses celcius read from max as input
```

```cpp
    Input = ktc.readCelsius();
    myPID.Compute();
    analogWrite(PIN_OUTPUT, Output);
    endtime = millis();
}

Serial.println("   ");
Serial.print("TMA Pulse no.     ");
Serial.println(i);
Serial.println("   ");

digitalWrite(valve3.pin, HIGH);
delay(valve3.valvedel);
digitalWrite(valve3.pin, LOW);

/////////Runs PID heater/////////////////////

starttime = millis();
endtime = starttime;
while ((endtime - starttime) <= valve1.pumptime)
{
    Serial.println(ktc.readCelsius());
    delay(200);
    //Uses celcius read from max as input
    Input = ktc.readCelsius();
    myPID.Compute();
    analogWrite(PIN_OUTPUT, Output);
    endtime = millis();
}


digitalWrite(valve1.pin, HIGH);
delay(valve1.valvedel);
digitalWrite(valve1.pin, LOW);

/////////Runs PID heater/////////////////////

starttime = millis();
endtime = starttime;
while ((endtime - starttime) <= valve1.pumptime)
{
    Serial.println(ktc.readCelsius());
    delay(200);
    //Uses celcius read from max as input
    Input = ktc.readCelsius();
    myPID.Compute();
    analogWrite(PIN_OUTPUT, Output);
    endtime = millis();
}

Serial.println("   ");
Serial.print("H20 Pulse no.     ");
Serial.println(i);
Serial.println("   ");

digitalWrite(valve2.pin, HIGH);
delay(valve2.valvedel);
digitalWrite(valve2.pin, LOW);


Serial.println('pulse number ');
```

```
        Serial.print(i);
      }
    }
    while (1 == 1) {
      Serial.println(ktc.readCelsius());
      delay(200);
      //Uses celcius read from max as input
      Input = ktc.readCelsius();
      myPID.Compute();
      analogWrite(PIN_OUTPUT, Output);
    }

}
```